Multi-robot Active Target Tracking with Combinations of Relative Observations

Ke Zhou and Stergios I. Roumeliotis
{kezhou|stergios}@cs.umn.edu

Department of Computer Science & Engineering
University of Minnesota

Multiple Autonomous
Robotic Systems Labroratory

Technical Report
Number -2010-004
April 2010

Dept. of Computer Science & Engineering
University of Minnesota
4-192 EE/CS Building
200 Union St. S.E.
Minneapolis, MN 55455
Tel: (612) 625-2217
Fax: (612) 625-0572

Multi-robot Active Target Tracking with Combinations of Relative Observations

Ke Zhou* and Stergios I. Roumeliotis†
*Dept. of Electrical and Computer Engineering, †Dept. of Computer Science and Engineering
University of Minnesota, Minneapolis, MN 55455 Email: {kezhou|stergios}@cs.umn.edu

***Abstract*—In this paper, we study the problem of *optimal trajectory generation* for a team of heterogeneous robots moving in a plane and tracking a moving target by processing *relative* observations, i.e., distance *and/or* bearing. Contrary to previous approaches, we explicitly consider limits on the robots' speed and impose constraints on the minimum distance at which the robots are allowed to approach the target. We first address the case of a single tracking sensor and seek the next sensing location in order to minimize the uncertainty about the target's position. We show that although the corresponding optimization problem involves a non-convex objective function and a non-convex constraint, its *global* optimal solution can be determined analytically. We then extend the approach to the case of multiple sensors and propose an iterative algorithm, *Gauss-Seidel-relaxation* (GSR), for determining the next best sensing location for each sensor. Extensive simulation results demonstrate that the GSR algorithm, whose computational complexity is *linear* in the number of sensors, achieves higher tracking accuracy than *gradient descent* methods, and has performance indistinguishable from that of a *grid-based exhaustive search*, whose cost is exponential in the number of sensors. Finally, through experiments we demonstrate that the proposed GSR algorithm is robust and applicable to real systems.**

***Index Terms*—Mobile Sensor, Target Tracking, Distance Measurement, Bearing Measurement, Gauss-Seidel Relaxation.**

I. Introduction

Optimally tracking a moving target under motion and processing constraints is necessary in a number of applications such as environmental monitoring [1], surveillance [2], [3], human-robot interaction [4], as well as defense applications [5]. In most cases in practice, multiple *static* wireless sensors are employed in order to improve the tracking accuracy and increase the size of the surveillance area. Contrary to static sensors, whose density and sensing range are fixed, *mobile* sensors (robots) can cover larger areas over time without the need to increase their number. Additionally, their spatial distribution can change dynamically so as to adapt to the target's motion, and hence provide informative measurements about its position. Selecting the *best sensing locations* is of particular importance especially when considering time-critical applications (e.g., when tracking a hostile target), as well as limitations on the robots' processing and communication resources.

In this paper, our objective is to determine optimal trajectories for a team of heterogeneous robots that track a moving target using a mixture of relative observations, including *distance-only*, *bearing-only*, and *distance-and-bearing* measurements. Since accurately predicting the motion of the target over multiple time steps is impossible, we focus our attention to the case where the robots must determine their optimal sensing locations for one step ahead at a time. Specifically, we seek to minimize the uncertainty about the position of the target, expressed as the trace of the posterior covariance matrix for the target's position estimates, while considering maximum-speed limitations on the robots' motion. Additionally, in order to avoid collisions, we impose constraints on the minimum distance between any of the robots and the target. This formulation results in a non-convex objective function with non-convex constraints on the optimization variables (i.e., the robots' sensing locations).

The main contributions of this work are the following:

- We first investigate the case of a *single sensor* and for the first time we prove that the global optimal solution to the active target tracking problem can be determined analytically for arbitrary target motion models. In particular, we show that depending on the distance between the robot and the target, two distinct cases must be considered, each corresponding to a different pair of polynomial equations in two variables, whose finite and discrete solution set contains the optimal solution.
- We extend the above approach to the case of *multiple heterogeneous sensors* by employing the non-linear Gauss-Seidel-relaxation (GSR) algorithm whose computational complexity is linear in the number of sensors. Additionally, we compare the performance of the GSR algorithm to that of a grid-based exhaustive search (GBES), whose cost is exponential in the number of sensors, and show that GSR achieves comparable tracking accuracy at a significantly lower computational cost. Moreover, we demonstrate that the GSR algorithm outperforms gradient-descent-based approaches and is significantly better compared to the case where the sensors simply follow the target.

Following a brief review of related work in Section II, we present the formulation of the target-tracking problem in Section III. In Section IV, the global optimal solution for a single sensor is determined analytically, while the non-linear GSR algorithm employed to solve the multiple-sensors case is described in Section V. Extensive simulation and real-world experimental results are presented in Sections VI and VII, respectively, while the conclusions of this work and directions of future research are discussed in Section VIII.

This work was supported by the University of Minnesota (DTC), and the National Science Foundation (IIS-0643680, IIS-0811946, IIS-0835637).

II. Literature Review

Although target tracking has received considerable attention, in most cases the sensors involved are *static* and the emphasis is on the optimal processing of the available information (e.g., given communication constraints [6]). In contrast to using *static* sensors, the deployment of *mobile* sensors (or *robots*) for tracking offers significant advantages. For example, a larger area can be covered without the need to increase the number of nodes in the sensing network. The idea of optimally choosing the mobile sensors' locations in order to maximize information gain (also known as adaptive sensing or active perception) has been applied to the problems of cooperative localization [7], simultaneous localization and mapping [8], parameter estimation [9], [10], and optimal sensor selection [11], [12]. In what follows, we review single- and multi-robot tracking approaches that use *distance-only*, *bearing-only*, or *both distance and bearing* measurements.

A. Active target tracking - distance-only observations

Yang *et al.* [13] present an active sensing strategy using distance-only measurements, where both the *trace* and the *determinant* of the target position estimates' covariance are considered as the objective functions. The authors propose a control law, with constant step size, based on the *gradient* of the cost function with respect to each sensor's coordinates.

In [14], Martínez and Bullo address the problem of optimal sensor placement and motion coordination strategies for *homogeneous* sensor networks using distance-only measurements, where the emphasis is on the optimal sensor *placement* for (non random) *static* target position estimation. The objective is to minimize the *determinant* of the covariance matrix. The resulting control law requires that the sensors move on a polygon surrounding the target so as the vectors from the target to the sensors are uniformly (in terms of direction) spaced.

Recently, Stump *et al.* [15] investigated the problem of localizing a *stationary* target by processing distance-only measurements from mobile sensors. The objective is to select the sensing locations such that the *time derivative* of the *determinant* of the target-position estimates' *information matrix* (i.e., the inverse of the covariance matrix) is maximized. The proposed control law is based on the *gradient* of the cost function with respect to each sensor's coordinates, and is implemented in a distributed fashion. Additionally, the expected distance measurements in the next time step are approximated by assuming that they will be the same as these recorded at the sensors' current locations.

B. Active target tracking - bearing-only observations

In [16], Le Cadre proposes an approximate tracking algorithm, in which a *single* mobile sensor attempts to minimize the target's location and velocity uncertainty over a finite time horizon, using bearing measurements. Under the assumption that the distance between the sensor and the target is *always constant*, the objective function (the *determinant* of the Fisher Information Matrix – FIM) is significantly simplified, and the resulting control law requires that the sensor switches its bearing rate between its upper and lower bound.

In contrast to [16], where the optimization is performed in the discrete time domain, Passerieux and Van Cappel [17] formulate the optimal trajectory generation for *single*-sensor target tracking using bearing measurements in continuous time. In this case, the target is constrained to move on a *straight line* with *constant velocity* and the objective is to minimize the target's location and velocity uncertainty by maximizing the FIMs' *determinant* over a finite time horizon. The authors present the *necessary* condition for the continuous-time optimal sensor path based on the Euler equation.

In [18], Logothetis *et al.* study the *single*-sensor trajectory optimization from an information theory perspective, where the sensor attempts to reduce the target's location and velocity uncertainty through bearing measurements. The authors employ the *determinant* of the target's covariance matrix over a finite time horizon as the cost function, and compute the optimal solution by performing a *grid-based exhaustive search*. Acknowledging that the computational requirements increase exponentially with *the number of time steps*, the authors present suboptimal solutions in [19], where the *grid-based minimization* takes place over only one time step.

Recently, Frew [20] investigates the problem of *single-sensor* trajectory generation for target tracking using bearing measurements. In this case, motion constraints on the sensor's trajectory are explicitly incorporated in the problem formulation and the objective function (*determinant* of the target's covariance matrix) is minimized over a finite time horizon using *exhaustive search* through a discretized set of candidate sensor headings.

C. Active target tracking - distance-and-bearing observations

Stroupe and Balch [21] propose an approximate tracking behavior, where the mobile sensors attempt to minimize the target's location uncertainty using distance-and-bearing measurements. The objective function is the *determinant* of the target position estimates' covariance matrix, and the optimization problem is solved by *greedy search* over the discretized set of candidate headings, separately for each sensor. Additionally, the expected information gain from the teammates' actions is approximated by assuming that their measurements in the next time step will be the same as these recorded at their current locations.

Olfati-Saber [22] addresses the problem of distributed target tracking for mobile sensor networks with a dynamic communication topology. The author tackles the network connectivity issue using a flocking-based mobility model, and presents a modified version of the distributed Kalman filter algorithm for estimating the target's state. In this case, the sensors use both distance and bearing measurements to a target that moves in 2D with constant velocity driven by zero-mean Gaussian noise, and seek to *minimize their distances* to the target, while avoiding collisions.

Chung *et al.* [23] present a decentralized motion planning algorithm for solving the multi-sensor target tracking problem using both distance and bearing measurements. The authors employ the *determinant* of the target's position covariance matrix as the cost function. The decentralized control law in

this case is based on the *gradient* of the cost function with respect to each of the sensor's coordinates with constant step-size of 1.

D. Summary

The main drawback of the previous approaches is that *no physical constraints* on the motion of the sensors are considered. The only exceptions are the works presented in [21] for distance-and-bearing observations, and in [20] for bearing-only observations. However, in both cases the proposed grid-based exhaustive search algorithm, when extended to the multi-sensor case, has computational complexity *exponential* in the number of sensors, which becomes prohibitive when the number of the sensors is large and/or the size of the grid cell is small. In addition, teams of heterogeneous sensors using mixed (i.e., distance and/or bearing) relative observations are only considered in [13], whose gradient-based algorithm can only guarantee achieving *local* minimum, while its convergence rate is not addressed. Moreover, analytical solutions for a single sensor tracking a moving target are provided only for the bearing-measurements case when the target is restricted either to be at a constant distance from the sensor [16], or to move on a straight line with constant velocity [17]. Lastly, extensions of [16] and [17] to multi-sensor target tracking have not been considered.

Compared to our previous work [24], where only distance observations were employed, in this paper, we address the most general case of active target tracking when processing a mixture of relative measurements (i.e., distance and/or bearing)[1]. Specifically, we first address the problem of single-sensor target tracking where we explicitly consider constraints on the robot's motion by imposing bounds on its maximum speed, as well as on the minimum distance between the robot and the target. However, contrary to [16] and [17], we require no particular type of target's motion. Our main contribution is that we derive the *global optimal solutions* for distance-only, bearing-only, and distance-and-bearing observations, analytically. Moreover, we generalize these results to the multi-sensor case by employing *Gauss-Seidel relaxation* that minimizes the trace of the target's position estimate covariance with respect to the motion of *all* sensors in a coordinate-descent fashion. Our algorithm applies to heterogeneous sensor teams using a mixture of observations, has computational complexity *linear* in the number of sensors, and achieves tracking accuracy indistinguishable of that of an exhaustive search over all possible combinations of the sensors' locations[2].

[1]Our previous publication [24] and the current paper share some parts of the problem formulation. However, our current work generalizes the results in [24] (which are applicable solely to the case of distance-only measurements) by providing solutions to distance-only, as well as bearing-only and distance-and-bearing observation models. Furthermore, for the single-sensor case, the solution strategies employed in [24] and in our current paper are fundamentally different. While the closed-form optimal solution in [24] is determined *geometrically*, our current work derives the optimal solution *algebraically* by solving the corresponding *KKT optimality conditions* analytically.

[2]A preliminary version of this paper was presented in [25] where all sensors can measure both distance and bearing to the target. This paper extends the results in [25] by providing a unified framework to characterize the solutions for the three different measurement models (i.e., distance-only, bearing-only, and distance-and-bearing), and is applicable to heterogeneous sensor teams which collect a mixture of observations.

III. Problem Formulation

Consider a group of mobile sensors (or robots) moving in a plane and tracking the position of a moving target by processing relative measurements, consisting of distance-only, bearing-only, and distance-and-bearing observations. In this paper, we study the case of *global tracking*, i.e., the position of the target is described with respect to a fixed (global) frame of reference, instead of a relative *group-centered* one. Hence, we hereafter employ the assumption that the position and orientation (pose) of each tracking sensor are known with high accuracy within the global frame of reference (e.g., from precise GPS and compass measurements).

Furthermore, we consider the case where each sensor moves in 2D with speed v_i, which is *upper bounded* by $v_{i\max}$, $i = 1, \ldots, M$, where M is the number of sensors. Therefore, at time-step $k+1$, sensor-i can only move within a circular region centered at its position at time-step k with radius $v_{i\max}\delta t$, where δt is the time step (see Fig. 1). In order to avoid collisions with the target, we also require that the distance between the target and sensor-i to be greater than a threshold ρ_i, i.e., sensor-i is prohibited to move inside a circular region centered at the target's position estimate[3] at time-step $k+1$ with radius ρ_i (see Fig. 1)[4]. Note also that since the motion of the target can be reliably predicted for the next time step only, our objective is to determine the next best sensing locations for all sensors at one time step ahead.

In the next two sections, we present the target's state propagation equations and the sensors' measurement models.

A. State Propagation

In this work, we employ the Extended Kalman Filter (EKF) for recursively estimating the target's state, $\mathbf{x}_T(k)$. This is defined as a vector of dimension $2N$, where $N-1$ is the highest-order time derivative of the target's position described by the motion model, and can include components such as position, velocity, and acceleration:

$$\mathbf{x}_T(k) = [\ x_T(k)\ y_T(k)\ \dot{x}_T(k)\ \dot{y}_T(k)\ \ddot{x}_T(k)\ \ddot{y}_T(k)\ \ldots\ ]^{\mathrm{T}} \quad (1)$$

We consider the case where the target moves randomly and assume that we know the stochastic model describing the motion of the target (e.g., constant-acceleration or constant-velocity, etc.). However, as it will become evident later on, our sensing strategy does not depend on the particular selection of the target's motion model.

The discrete-time state propagation equation is:

$$\mathbf{x}_T(k+1) = \mathbf{\Phi}_k \mathbf{x}_T(k) + \mathbf{G}_k \mathbf{w}_d(k) \quad (2)$$

[3]Ideally, the collision-avoidance constraints should be defined using the *true* position of the target. However, since true target position is *unavailable*, we instead use the *estimated* target position and appropriately increase the safety distance to account for the uncertainty in this estimate.

[4]As explained in Section IV-E, our problem formulation can be extended to handle additional motion constraints such as those imposed by obstacles or the sensors' kinematics, e.g., maximum turning rates imposed on the sensors' motion directions. The effect of these will change the shape of the feasible set from a circular disk to an area determined by the turning-radius constraints. Note, however, that this new region can also be described by polynomial constraints, since the kinematics of a mobile robot involve sine and cosine functions.

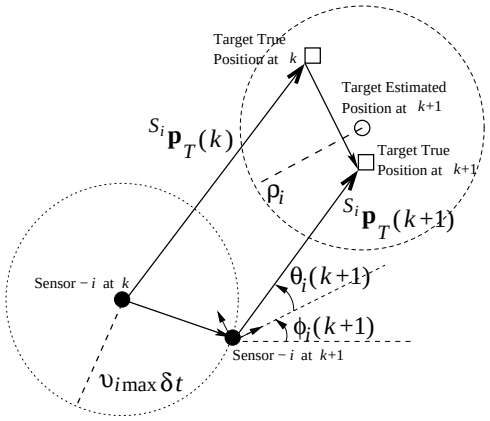

Fig. 1. Illustration of the i-th sensor's and target's motion: Sensor-i moves in 2D with speed v_i, which is bounded by $v_{i\max}$. From time-step k to $k+1$, the sensor can only move *within* a circular region centered at its position at time-step k with radius $v_{i\max}\delta t$. Furthermore, to avoid collision with the target, sensor-i is prohibited to move inside a circular region centered at the target's position *estimate* at time-step $k+1$ with radius ρ_i. ${}^{S_i}\mathbf{p}_T$ is the target's position with respect to sensor-i. The distance measurement of sensor-i is the norm of ${}^{s_i}\mathbf{p}_T(k+1)$ plus noise, and the bearing measurement of sensor-i is $\theta_i(k+1)$ plus noise.

where $\mathbf{w}_d$ is a zero-mean white Gaussian noise process with covariance $\mathbf{Q}_d = \mathbb{E}[\mathbf{w}_d(k)\mathbf{w}_d^{\mathrm{T}}(k)]$. The state transition matrix, $\mathbf{\Phi}_k$, and the process noise Jacobian, $\mathbf{G}_k$, that appear in (2) depend on the motion model used [26]. In our work, these can be *arbitrary*, but *known*, matrices, since no assumptions on their properties are imposed.

The estimate of the target's state is propagated by:[5]

$$\hat{\mathbf{x}}_T(k+1|k) = \mathbf{\Phi}_k\hat{\mathbf{x}}_T(k|k) \tag{3}$$

where $\hat{\mathbf{x}}_T(\ell|j)$ is the state estimate at time-step ℓ, after measurements up to time-step j have been processed.

The error-state covariance matrix is propagated as:

$$\mathbf{P}_{k+1|k} = \mathbf{\Phi}_k\mathbf{P}_{k|k}\mathbf{\Phi}_k^{\mathrm{T}} + \mathbf{G}_k\mathbf{Q}_d\mathbf{G}_k^{\mathrm{T}}$$

where $\mathbf{P}_{\ell|j}$ is the covariance of the error, $\tilde{\mathbf{x}}_T(\ell|j) = \mathbf{x}_T(\ell) - \hat{\mathbf{x}}_T(\ell|j)$, in the state estimate.

B. Measurement Model

Let us denote the complete set of the sensor team as $\mathcal{M} = \{1, \ldots, M\}$, where M is the number of the sensors. At time-step $k+1$, based on the type of the measurement that each sensor collects, $\mathcal{M}$ can be partitioned into $\mathcal{M}_1 \cup \mathcal{M}_2 \cup \mathcal{M}_3$, where $\mathcal{M}_1$ denotes the set of sensors that have access to both distance and bearing observations; $\mathcal{M}_2$ comprises sensors that measure only bearing; and $\mathcal{M}_3$ consists of sensors that record distance-only measurements. In what follows, $\mathbf{p}_T(k+1) = [x_T(k+1)\ y_T(k+1)]^{\mathrm{T}}$ and $\mathbf{p}_{S_i}(k+1) = [x_{S_i}(k+1)\ y_{S_i}(k+1)]^{\mathrm{T}}$ denote the positions of the target and the i-th sensor, respectively, expressed in the global frame of reference. Furthermore, to simplify the notation, we introduce the following quantities ($i = 1, \ldots, M$):

$$\begin{aligned}
\Delta x_{T_i}(k+1) &= x_T(k+1) - x_{S_i}(k+1)\\
\Delta y_{T_i}(k+1) &= y_T(k+1) - y_{S_i}(k+1)\\
\widehat{\Delta x}_{T_i}(k+1|k) &= \hat{x}_T(k+1|k) - x_{S_i}(k+1)\\
\widehat{\Delta y}_{T_i}(k+1|k) &= \hat{y}_T(k+1|k) - y_{S_i}(k+1)\\
\mathbf{p}_i &= \mathbf{p}_i(k+1) = \mathbf{p}_{S_i}(k+1) - \hat{\mathbf{p}}_T(k+1|k)
\end{aligned} \tag{4}$$

1) Distance-and-Bearing Observation Model: At time-step $k+1$, sensor-j ($j \in \mathcal{M}_1$) records its distance-and-bearing observations [$d_j(k+1)$ and $\theta_j(k+1)$] to the target, as shown in Fig. 1. The measurement equation is:

$$\mathbf{z}_j(k+1) = \begin{bmatrix} d_j(k+1)\\ \theta_j(k+1)\end{bmatrix} + \begin{bmatrix} n_{d_j}(k+1)\\ n_{\theta_j}(k+1)\end{bmatrix} \tag{5}$$

with

$$d_j(k+1) = \sqrt{\Delta x_{T_j}^2(k+1) + \Delta y_{T_j}^2(k+1)} \tag{6}$$

$$\theta_j(k+1) = \arctan\left(\frac{\Delta y_{T_j}(k+1)}{\Delta x_{T_j}(k+1)}\right) - \phi_j(k+1) \tag{7}$$

where $\phi_j(k+1)$ is the orientation of sensor-j, and $\mathbf{n}_j(k+1) = \left[n_{d_j}(k+1)\ n_{\theta_j}(k+1)\right]^{\mathrm{T}}$ is the noise in the j-th sensor's measurements, which is a zero-mean white Gaussian process with covariance $\mathbf{R}_j = \mathbb{E}[\mathbf{n}_j(k+1)\mathbf{n}_j^{\mathrm{T}}(k+1)] = \mathrm{diag}(\sigma_{d_j}^2, \sigma_{\theta_j}^2)$, and independent of the noise in other sensors, i.e., $\mathbb{E}[\mathbf{n}_j(k+1)\mathbf{n}_i^{\mathrm{T}}(k+1)] = \mathbf{0}$ for $i \neq j$.

The measurement of sensor-j is a nonlinear function of the state variable $\mathbf{x}_T$ [see (5)]. The measurement-error equation for sensor-j, obtained by linearizing (5) is:

$$\begin{aligned}
\tilde{\mathbf{z}}_j(k+1|k) &= \mathbf{z}_j(k+1) - \hat{\mathbf{z}}_j(k+1|k)\\
&\simeq \mathbf{H}_{k+1}^{(j)}\tilde{\mathbf{x}}_T(k+1|k) + \mathbf{n}_j(k+1)
\end{aligned} \tag{8}$$

where

$$\hat{\mathbf{z}}_j(k+1|k) = [\hat{d}_j(k+1|k)\ \ \hat{\theta}_j(k+1|k)]^{\mathrm{T}}$$

$$\hat{d}_j(k+1|k) = \sqrt{\widehat{\Delta x}_{T_j}^2(k+1|k) + \widehat{\Delta y}_{T_j}^2(k+1|k)}$$

$$\hat{\theta}_j(k+1|k) = \arctan\left(\frac{\widehat{\Delta y}_{T_j}(k+1|k)}{\widehat{\Delta x}_{T_j}(k+1|k)}\right) - \phi_j(k+1)$$

Note that the measurement matrix in (8) has a block column structure, which is given by the following expression:

$$\mathbf{H}_{k+1}^{(j)} = \begin{bmatrix}\mathbf{h}_j^{\mathrm{T}}(k+1) & \mathbf{0}_{2\times(2N-2)}\end{bmatrix} \tag{9}$$

where $2N$ is the dimension of the state vector and

$$\mathbf{h}_j(k+1) = \begin{bmatrix}\mathbf{h}_{d_j}(k+1) & \mathbf{h}_{\theta_j}(k+1)\end{bmatrix} \tag{10}$$

$$\mathbf{h}_{d_j}(k+1) = \frac{-1}{\sqrt{\mathbf{p}_j^{\mathrm{T}}\mathbf{p}_j}}\mathbf{p}_j\ ,\ \mathbf{h}_{\theta_j}(k+1) = \frac{1}{\mathbf{p}_j^{\mathrm{T}}\mathbf{p}_j}\mathbf{J}\mathbf{p}_j \tag{11}$$

where $\mathbf{J} = \mathbf{C}\left(-\frac{\pi}{2}\right)$ and $\mathbf{C}(\cdot)$ is the 2×2 rotational matrix.

2) Bearing-only Observation Model: At time-step $k+1$, sensor-ℓ ($\ell \in \mathcal{M}_2$) only has access to its bearing measurement $\theta_\ell(k+1)$ towards the target [see (7)], and the measurement

[5] In the remainder of the paper, the "hat" symbol, $\hat{}$, denotes the estimated value of a quantity, while the "tilde" symbol, $\tilde{}$, represents the error between the actual value of a quantity and its estimate. The relationship between a variable, x, and its estimate, $\hat{x}$, is $\tilde{x} = x - \hat{x}$. Additionally, "$\succ$" and "$\succeq$" denote the matrix inequality in the positive definite and positive semidefinite sense, respectively. $\mathbf{0}_{m\times n}$ and $\mathbf{I}_n$ represent the $m\times n$ zero matrix and $n\times n$ identity matrix, respectively.

and measurement-error equations are:

$$\begin{aligned}\mathbf{z}_\ell(k+1) &= \theta_\ell(k+1) + n_{\theta_\ell}(k+1)\\ \tilde{\mathbf{z}}_\ell(k+1|k) &\simeq \mathbf{H}_{k+1}^{(\ell)}\tilde{\mathbf{x}}_T(k+1|k) + \mathbf{n}_\ell(k+1)\end{aligned} \tag{12}$$

where $\mathbf{n}_\ell(k+1) = n_{\theta_\ell}(k+1)$ is the zero-mean white Gaussian measurement noise with variance $\mathbf{R}_\ell = \mathbb{E}[\mathbf{n}_\ell(k+1)\mathbf{n}_\ell^{\mathrm{T}}(k+1)] = \sigma_{\theta_\ell}^2$, which is independent of the noise in other sensors. As before, the measurement matrix $\mathbf{H}_{k+1}^{(\ell)}$ has the following structure:

$$\mathbf{H}_{k+1}^{(\ell)} = \begin{bmatrix}\mathbf{h}_\ell^{\mathrm{T}}(k+1) & \mathbf{0}_{1\times(2N-2)}\end{bmatrix} \tag{13}$$

$$\mathbf{h}_\ell(k+1) = \mathbf{h}_{\theta_\ell}(k+1) = \frac{1}{\mathbf{p}_\ell^{\mathrm{T}}\mathbf{p}_\ell}\mathbf{J}\mathbf{p}_\ell \tag{14}$$

3) Distance-only Observation Model: At time-step $k+1$, sensor-ι ($\iota \in \mathcal{M}_3$) only measures its distance $d_\iota(k+1)$ to the target [see (6)], therefore the measurement equation is:

$$\mathbf{z}_\iota(k+1) = d_\iota(k+1) + n_{d_\iota}(k+1)$$

and the corresponding measurement-error equation is:

$$\tilde{\mathbf{z}}_\iota(k+1|k) \simeq \mathbf{H}_{k+1}^{(\iota)}\tilde{\mathbf{x}}_T(k+1|k) + \mathbf{n}_\iota(k+1) \tag{15}$$

where $\mathbf{n}_\iota(k+1) = n_{d_\iota}(k+1)$ is the noise in the ι-th sensor's distance measurement, which is a zero-mean white Gaussian process with variance $\mathbf{R}_\iota = \mathbb{E}[\mathbf{n}_\iota(k+1)\mathbf{n}_\iota^{\mathrm{T}}(k+1)] = \sigma_{d_\iota}^2$, and independent of the noise in other sensors. Additionally, the measurement matrix $\mathbf{H}_{k+1}^{(\iota)}$ in (15) is given by the following expression:

$$\mathbf{H}_{k+1}^{(\iota)} = \begin{bmatrix}\mathbf{h}_\iota^{\mathrm{T}}(k+1) & \mathbf{0}_{1\times(2N-2)}\end{bmatrix} \tag{16}$$

$$\mathbf{h}_\iota(k+1) = \mathbf{h}_{d_\iota}(k+1) = \frac{-1}{\sqrt{\mathbf{p}_\iota^{\mathrm{T}}\mathbf{p}_\iota}}\mathbf{p}_\iota \tag{17}$$

4) Linearized Measurement-Error Equation: The overall measurement-error equation at time-step $k+1$, obtained by stacking all measurement-error equations corresponding to each sensor [see (8), (12), and (15)], is:

$$\begin{aligned}\tilde{\mathbf{z}}(k+1|k) &= \begin{bmatrix}\tilde{\mathbf{z}}_1^{\mathrm{T}}(k+1|k) & \dots & \tilde{\mathbf{z}}_M^{\mathrm{T}}(k+1|k)\end{bmatrix}^{\mathrm{T}}\\ &\simeq \mathbf{H}_{k+1}\tilde{\mathbf{x}}_T(k+1|k) + \mathbf{n}(k+1)\end{aligned}$$

with

$$\mathbf{n}(k+1) = \begin{bmatrix}\mathbf{n}_1^{\mathrm{T}}(k+1) & \dots & \mathbf{n}_M^{\mathrm{T}}(k+1)\end{bmatrix}^{\mathrm{T}}$$

and [see (9), (13), and (16)]

$$\mathbf{H}_{k+1} = \begin{bmatrix}\left(\mathbf{H}_{k+1}^{(1)}\right)^{\mathrm{T}} & \dots & \left(\mathbf{H}_{k+1}^{(M)}\right)^{\mathrm{T}}\end{bmatrix}^{\mathrm{T}} = \begin{bmatrix}\mathbf{H}_{e,k+1} & \mathbf{0}\end{bmatrix}$$

where $\mathbf{H}_{e,k+1}$ is the block element of the measurement matrix corresponding to the target's position:

$$\mathbf{H}_{e,k+1}^{\mathrm{T}} = \begin{bmatrix}\mathbf{h}_1(k+1) & \dots & \mathbf{h}_M(k+1)\end{bmatrix} \tag{18}$$

where $\mathbf{h}_i(k+1)$, $i = 1,\dots,M$, are defined based on the type of the observations considered [see (10), (14), and (17)]. Note also that $\mathbf{R} = \mathbb{E}[\mathbf{n}(k+1)\mathbf{n}^{\mathrm{T}}(k+1)] = \mathrm{diag}(\mathbf{R}_i)$, $i = 1,\dots,M$, due to the independence of the noise in each sensor.

C. State and Covariance Update

Once the measurements, $\mathbf{z}_i(k+1),\ i = 1,\dots,M$, from all the sensors are available, they are transmitted and processed at a fusion center (e.g., one of the robots in the team), and the target's state estimate and its covariance are updated as:

$$\begin{aligned}\hat{\mathbf{x}}_T(k+1|k+1) &= \hat{\mathbf{x}}_T(k+1|k) + \mathbf{K}_{k+1}\tilde{\mathbf{z}}(k+1|k)\\ \mathbf{P}_{k+1|k+1} &= \mathbf{P}_{k+1|k} - \mathbf{K}_{k+1}\mathbf{S}_{k+1}\mathbf{K}_{k+1}^{\mathrm{T}}\end{aligned} \tag{19}$$

where $\mathbf{K}_{k+1} = \mathbf{P}_{k+1|k}\mathbf{H}_{k+1}^{\mathrm{T}}\mathbf{S}_{k+1}^{-1}$ is the Kalman gain, and $\mathbf{S}_{k+1} = \mathbf{H}_{k+1}\mathbf{P}_{k+1|k}\mathbf{H}_{k+1}^{\mathrm{T}} + \mathbf{R}$ is the measurement residual covariance.

Our objective in this work is to determine the active-sensing strategy that minimizes the uncertainty for the *position* estimate of the target. In order to account for the impact of the prior state estimates on the motion of the sensors, we first present the following lemma.

Lemma 1: The posterior (updated) covariance for the target's position estimate depends on (i) the measurement sub-matrix corresponding to the target's *position*, and (ii) the prior (propagated) covariance sub-matrix of the target's *position*:

$$\mathbf{P}_{k+1|k+1,11} = \left(\left(\mathbf{P}_{k+1|k,11}\right)^{-1} + \mathbf{H}_{e,k+1}^{\mathrm{T}}\mathbf{R}^{-1}\mathbf{H}_{e,k+1}\right)^{-1} \tag{20}$$

where $\mathbf{H}_{e,k+1}$ is defined in (18) and $\mathbf{P}_{\ell|j,11}$ denotes the 2×2 upper diagonal sub-matrix of $\mathbf{P}_{\ell|j}$ [see (19)] corresponding to the covariance in the position estimates.

Proof: The proof is shown in Appendix A. ■

The importance of this lemma is that the optimization algorithms presented in Sections IV-V can be derived based on (20) for the position covariance update – instead of (19) for the entire state covariance update – regardless of the stochastic process model employed for describing the target's motion.

Exploiting the fact that $\mathbf{R}$ is diagonal, and substituting (18) into (20), we obtain the following expression for $\mathbf{P}_{k+1|k+1,11}$:

$$\begin{aligned}\mathbf{P}_{k+1|k+1,11} = \Bigg[&\left(\mathbf{P}_{k+1|k,11}\right)^{-1} + \sum_{j\in\mathcal{M}_1}\left(\frac{1}{\sigma_{d_j}^2}\frac{\mathbf{p}_j\mathbf{p}_j^{\mathrm{T}}}{\mathbf{p}_j^{\mathrm{T}}\mathbf{p}_j} + \frac{1}{\sigma_{\theta_j}^2}\frac{\mathbf{J}\mathbf{p}_j\mathbf{p}_j^{\mathrm{T}}\mathbf{J}^{\mathrm{T}}}{(\mathbf{p}_j^{\mathrm{T}}\mathbf{p}_j)^2}\right)\\ &+ \sum_{\ell\in\mathcal{M}_2}\frac{1}{\sigma_{\theta_\ell}^2}\frac{\mathbf{J}\mathbf{p}_\ell\mathbf{p}_\ell^{\mathrm{T}}\mathbf{J}^{\mathrm{T}}}{(\mathbf{p}_\ell^{\mathrm{T}}\mathbf{p}_\ell)^2} + \sum_{\iota\in\mathcal{M}_3}\frac{1}{\sigma_{d_\iota}^2}\frac{\mathbf{p}_\iota\mathbf{p}_\iota^{\mathrm{T}}}{\mathbf{p}_\iota^{\mathrm{T}}\mathbf{p}_\iota}\Bigg]^{-1}\end{aligned} \tag{21}$$

In order to encapsulate all three measurement models (see Section III-B) into a unified framework, we introduce two binary variables $\kappa_{d_i} \in \{0,1\}$ and $\kappa_{\theta_i} \in \{0,1\}$ for sensor-i, $i = 1,\dots,M$. $\kappa_{d_i} = 1$ if sensor-i can measure relative distance at time-step $k+1$, otherwise $\kappa_{d_i} = 0$; similarly, $\kappa_{\theta_i} = 1$ if sensor-i is capable of taking a bearing observation at time-step $k+1$, otherwise $\kappa_{\theta_i} = 0$. Following this convention, we have $\kappa_{d_i} = \kappa_{\theta_i} = 1,\ \forall i \in \mathcal{M}_1$; $\kappa_{d_i} = 0,\ \kappa_{\theta_i} = 1,\ \forall i \in \mathcal{M}_2$; $\kappa_{d_i} = 1,\ \kappa_{\theta_i} = 0,\ \forall i \in \mathcal{M}_3$. Using this convention, (21) can be written as:

$$\begin{aligned}&\mathbf{P}_{k+1|k+1,11}\\ &= \left(\left(\mathbf{P}_{k+1|k,11}\right)^{-1} + \sum_{i=1}^{M}\frac{\kappa_{d_i}}{\sigma_{d_i}^2}\frac{\mathbf{p}_i\mathbf{p}_i^{\mathrm{T}}}{\mathbf{p}_i^{\mathrm{T}}\mathbf{p}_i} + \sum_{i=1}^{M}\frac{\kappa_{\theta_i}}{\sigma_{\theta_i}^2}\frac{\mathbf{J}\mathbf{p}_i\mathbf{p}_i^{\mathrm{T}}\mathbf{J}^{\mathrm{T}}}{(\mathbf{p}_i^{\mathrm{T}}\mathbf{p}_i)^2}\right)^{-1}\end{aligned} \tag{22}$$

Remark 1: Note that $\forall i \in \mathcal{M}_2$, the term $\sigma_{d_i}^2$ is irrelevant, i.e., $\sigma_{d_i}^2$ can be set to any positive real number, since $\kappa_{d_i}\sigma_{d_i}^{-2} = 0$ regardless of the specific value of $\sigma_{d_i}^2$. Similarly, $\sigma_{\theta_i}^2$ is irrelevant $\forall i \in \mathcal{M}_3$.

Remark 2: When sensor-i is unable to detect the target and hence records neither distance nor bearing observations at time-step $k+1$, the corresponding κ_{d_i} and κ_{θ_i} in (22) are set to zero. In this case, the target's position posterior covariance is independent of the variable $\mathbf{p}_i$. However, we still require that sensor-i minimizes its distance ($\|\mathbf{p}_i\|$) to the estimated target location, while adhering to its motion and collision-avoidance constraints, so as to increase its probability of re-detecting the target in the following time steps. The updated estimate of the target's state $\hat{\mathbf{x}}_T(k+1|k+1)$ is communicated to sensor-i by those sensors that are able to detect and take relative measurements at time-step $k+1$. In case none of the robots can detect the target, i.e., $\kappa_{d_i} = \kappa_{\theta_i} = 0,\ \forall\ i \in \mathcal{M}$, then all robots propagate the previous state estimate [see (3)], and plan their motions so as to minimize their distances from the predicted target's location.

In the next section, we formulate the sensors' one-step-ahead *optimal motion strategy* as a constrained optimization problem, and discuss its properties.

D. Problem Statement and Reformulation

As is evident from (4) and (22), after each update step the target's position covariance matrix will depend, through $\mathbf{p}_i$, on all the next sensors' positions $\mathbf{p}_{S_i}(k+1) = [x_{S_i}(k+1)\ y_{S_i}(k+1)]^{\mathrm{T}},\ i = 1, \ldots, M$. Assume that at time-step k, sensor-i is located at $\mathbf{p}_{S_i}(k) = [x_{S_i}(k)\ y_{S_i}(k)]^{\mathrm{T}}$. At time-step $k+1$ its position $\mathbf{p}_{S_i}(k+1)$ is confined within a circular region centered at $\mathbf{p}_{S_i}(k)$, due to the maximum-speed constraint, but outside a circular region centered at $\hat{\mathbf{p}}_T(k+1|k)$ so as to avoid collisions (see Fig. 1), i.e.,

$$\|\mathbf{p}_{S_i}(k+1) - \mathbf{p}_{S_i}(k)\| \leq r_i \tag{23}$$

$$\|\mathbf{p}_{S_i}(k+1) - \hat{\mathbf{p}}_T(k+1|k)\| \geq \rho_i \tag{24}$$

where $r_i := \min\left(v_{i\max}\delta t, \|\mathbf{p}_{S_i}(k) - \hat{\mathbf{p}}_T(k+1|k)\|\right) \leq v_{i\max}\delta t,\ i = 1, \ldots, M$.

Substituting $\mathbf{p}_i$ [see (4)] in the above two inequalities, yields:

$$\left\|\mathbf{p}_i - [\mathbf{p}_{S_i}(k) - \hat{\mathbf{p}}_T(k+1|k)]\right\| \leq r_i \tag{25}$$

$$\|\mathbf{p}_i\| \geq \rho_i \tag{26}$$

thus, the feasible region of $\mathbf{p}_i$ is inside a circle of radius r_i centered at $\mathbf{p}_{S_i}(k) - \hat{\mathbf{p}}_T(k+1|k)$, and outside a circle of radius ρ_i centered at the origin $[0\ 0]^{\mathrm{T}}$. Note that the estimate $\hat{\mathbf{p}}_T(k+1|k)$ [see (3)] is shared among all sensors, and can be treated as a constant at time-step $k+1$. Hence, once $\mathbf{p}_i,\ i = 1, \ldots, M$, is determined, the location of sensor-i at time-step $k+1$, $\mathbf{p}_{S_i}(k+1),\ i = 1, \ldots, M$, can be obtained through (4).

The problem we address in this work is that of determining the sensors' *optimal motion strategy*, i.e., the set $\{\mathbf{p}_i,\ i = 1, \ldots, M\}$, that minimizes the *trace* of the target's position estimate covariance matrix [see (22)], under the constraints specified in (25)-(26):

- OPTIMIZATION PROBLEM 1 (Π_1)

$$\min_{\mathbf{p}_1, \ldots, \mathbf{p}_M} \operatorname{tr}\left(\left(\mathbf{P}_{k+1|k,11}\right)^{-1} + \sum_{i=1}^{M} \frac{\kappa_{d_i}}{\sigma_{d_i}^2} \frac{\mathbf{p}_i\mathbf{p}_i^{\mathrm{T}}}{\mathbf{p}_i^{\mathrm{T}}\mathbf{p}_i} + \sum_{i=1}^{M} \frac{\kappa_{\theta_i}}{\sigma_{\theta_i}^2} \frac{\mathbf{J}\mathbf{p}_i\mathbf{p}_i^{\mathrm{T}}\mathbf{J}^{\mathrm{T}}}{(\mathbf{p}_i^{\mathrm{T}}\mathbf{p}_i)^2}\right)^{-1}$$

$$\text{s.t. } \left\|\mathbf{p}_i - [\mathbf{p}_{S_i}(k) - \hat{\mathbf{p}}_T(k+1|k)]\right\| \leq r_i, \quad \|\mathbf{p}_i\| \geq \rho_i, \quad i = 1, \ldots, M \tag{27}$$

In what follows, we apply a coordinate transformation (see Lemma 2), to convert the objective function of Π_1 into (28), in which $\mathbf{\Lambda}$ is a diagonal matrix.

Lemma 2: Assume $\mathbf{P}_{k+1|k,11} \succ \mathbf{0}_{2\times 2}$ is non-diagonal, and consider the eigen-decomposition $\mathbf{P}_{k+1|k,11}^{-1} = \mathbf{C}(\varphi_0)\mathbf{\Lambda}\mathbf{C}(-\varphi_0)$, where $\mathbf{\Lambda} = \operatorname{diag}(\lambda_1^{-1}, \lambda_2^{-1})$ and $\lambda_1 \geq \lambda_2 > 0$. Then

$$\operatorname{tr}(\mathbf{P}_{k+1|k+1,11}) = \operatorname{tr}\left(\mathbf{\Lambda} + \sum_{i=1}^{M} \frac{\kappa_{d_i}}{\sigma_{d_i}^2} \frac{\mathbf{s}_i\mathbf{s}_i^{\mathrm{T}}}{\mathbf{s}_i^{\mathrm{T}}\mathbf{s}_i} + \sum_{i=1}^{M} \frac{\kappa_{\theta_i}}{\sigma_{\theta_i}^2} \frac{\mathbf{J}\mathbf{s}_i\mathbf{s}_i^{\mathrm{T}}\mathbf{J}^{\mathrm{T}}}{(\mathbf{s}_i^{\mathrm{T}}\mathbf{s}_i)^2}\right)^{-1} \tag{28}$$

where $\mathbf{s}_i = \mathbf{C}(-\varphi_0)\mathbf{p}_i,\ i = 1, \ldots, M$.

Proof: Substituting $\mathbf{P}_{k+1|k,11}^{-1} = \mathbf{C}(\varphi_0)\mathbf{\Lambda}\mathbf{C}(-\varphi_0)$ and $\mathbf{p}_i = \mathbf{C}(\varphi_0)\mathbf{s}_i$ in (27), employing the equality $\mathbf{C}(-\varphi_0)\mathbf{J} = \mathbf{J}\mathbf{C}(-\varphi_0)$ which holds since both are 2×2 rotational matrices, and noting that the trace operation is invariant to similarity transformations results in (28). ∎

Note also that the similarity transformation does not change the norm of a vector; thus, constraint (25) is equivalent to $\|\mathbf{s}_i - \mathbf{c}_i\| \leq r_i$, with $\mathbf{c}_i = \mathbf{C}(-\varphi_0)\left[\mathbf{p}_{S_i}(k) - \hat{\mathbf{p}}_T(k+1|k)\right]$, and constraint (26) is equivalent to $\|\mathbf{s}_i\| \geq \rho_i$. Therefore, Π_1 is equivalent to the following optimization problem:

- OPTIMIZATION PROBLEM 2 (Π_2)

$$\min_{\mathbf{s}_1, \ldots, \mathbf{s}_M} \operatorname{tr}\left(\mathbf{\Lambda} + \sum_{i=1}^{M} \frac{\kappa_{d_i}}{\sigma_{d_i}^2} \frac{\mathbf{s}_i\mathbf{s}_i^{\mathrm{T}}}{\mathbf{s}_i^{\mathrm{T}}\mathbf{s}_i} + \sum_{i=1}^{M} \frac{\kappa_{\theta_i}}{\sigma_{\theta_i}^2} \frac{\mathbf{J}\mathbf{s}_i\mathbf{s}_i^{\mathrm{T}}\mathbf{J}^{\mathrm{T}}}{(\mathbf{s}_i^{\mathrm{T}}\mathbf{s}_i)^2}\right)^{-1} \tag{29}$$

$$\text{s.t. } \|\mathbf{s}_i - \mathbf{c}_i\|^2 \leq r_i^2, \tag{30}$$

$$\|\mathbf{s}_i\|^2 \geq \rho_i^2, \qquad i = 1, \ldots, M \tag{31}$$

Once the optimal solution $\{\mathbf{s}_i,\ i = 1, \ldots, M\}$ is obtained, the best sensing location for sensor-i at time-step $k+1$, $\mathbf{p}_{S_i}(k+1)$, can be calculated through $\mathbf{p}_i = \mathbf{C}(\varphi_0)\mathbf{s}_i$ and (4).

Remark 3: The optimization problem Π_2 is a nonlinear programming problem since both the objective function [see (29)] and constraints [see (30)-(31)] are nonlinear functions with respect to the optimization variable $\mathbf{s} = \left[\mathbf{s}_1^{\mathrm{T}}\ \ldots\ \mathbf{s}_M^{\mathrm{T}}\right]^{\mathrm{T}}$. Moreover, Π_2 (and equivalently, Π_1) is not a convex program since the objective function (29) is non-convex with respect to $\mathbf{s}$, and the feasible set defined by constraint (31) is not convex.

Remark 4: As shown in [24], given distance-only observations, the corresponding optimization problem, when considering maximum-speed constraints, is *NP-Hard*. Thus the more general problem addressed in this paper (of which [24] is a special case) is also *NP-Hard* in general.

The above remark establishes the fact that the problem of *optimal trajectory generation* for multiple sensors with mobility constraints that track a moving target using mixed relative observations (i.e., distance and/or bearing), is *NP-Hard* in general. Hence, finding the *global* optimal solution for Π_1 or Π_2 is extremely challenging. Ideally, the optimal solution can be determined if one discretizes the feasible set of all sensors [see (30)-(31)] and performs an exhaustive search. This approach, however, has computational complexity *exponential* in the number of sensors, which is of limited practical use given realistic processing constraints.

In order to design algorithms that can operate in real time, appropriate relaxations of Π_2 become necessary. In what

follows, we first derive the analytic solution for the single-sensor case (see Section IV) and based on that we propose a *Gauss-Seidel relaxation* (GSR) to solve the general problem of multiple sensors (see Section V), which has computational complexity *linear* in the number of sensors.

IV. Single-sensor Active Target Tracking: Analytical Solution

For $M = 1$, the optimization problem Π_2 described by (29)-(31) is simplified to:[6]

- Optimization Problem 3 (Π_3)

$$\min_{\mathbf{s}} \quad f_0(\mathbf{s}) = \operatorname{tr}\left(\mathbf{\Lambda} + \frac{\kappa_d}{\sigma_d^2}\frac{\mathbf{s}\mathbf{s}^{\mathrm{T}}}{\mathbf{s}^{\mathrm{T}}\mathbf{s}} + \frac{\kappa_\theta}{\sigma_\theta^2}\frac{\mathbf{J}\mathbf{s}\mathbf{s}^{\mathrm{T}}\mathbf{J}^{\mathrm{T}}}{(\mathbf{s}^{\mathrm{T}}\mathbf{s})^2}\right)^{-1} \tag{32}$$

$$\text{s.t.} \quad \|\mathbf{s}-\mathbf{c}\|^2 \le r^2, \tag{33}$$

$$\|\mathbf{s}\|^2 \ge \rho^2 \tag{34}$$

In order to solve Π_3, we proceed as follows: We first determine *all critical/stationary points* (i.e., those points which satisfy the Karush-Kuhn-Tucker (KKT) necessary optimality conditions [27, Ch. 3]) analytically and evaluate their objective values. Then, as optimal solution for Π_3 we select the critical point whose objective value is the smallest.

To proceed, we first construct the Lagrange function [27]:

$$L(\mathbf{s},\mu,\nu) = f_0(\mathbf{s}) + \frac{\mu}{2}\left(\|\mathbf{s}-\mathbf{c}\|^2 - r^2\right) + \frac{\nu}{2}\left(\rho^2 - \|\mathbf{s}\|^2\right)$$

Based on the KKT necessary conditions, the critical points $\mathbf{s}^*$, and the associated Lagrange multipliers μ^* and ν^*, must satisfy:

$$\nabla f_0(\mathbf{s}^*) + \mu^*(\mathbf{s}^*-\mathbf{c}) - \nu^*\mathbf{s}^* = \mathbf{0}_{2\times 1} \tag{35}$$

$$\mu^* \ge 0, \quad \mu^*\left(\|\mathbf{s}^*-\mathbf{c}\|^2 - r^2\right) = 0 \tag{36}$$

$$\nu^* \ge 0, \quad \nu^*\left(\rho^2 - \|\mathbf{s}^*\|^2\right) = 0 \tag{37}$$

Clearly (36)-(37) are degree-3 multivariate *polynomial* equations in the unknowns $\mathbf{s}^*$, μ^* and ν^*. Furthermore, as shown in Appendix B, both f_0 and its derivative ∇f_0 are *rational* functions with respect to $\mathbf{s}^*$, and thus (35) can be transformed into a *polynomial* equality in $\mathbf{s}^*$, μ^*, and ν^*. Therefore, computing all critical points of Π_3 is equivalent to solving the polynomial system defined by (35)-(37). Moreover, it is worth mentioning that unlike linear systems, in general there exist *multiple solutions* for the above polynomial system. In order to efficiently solve (35)-(37), we first prove the following lemma:

Lemma 3: Assume $\bar{\Omega} = \Omega \cup \partial\Omega$ is a compact and connected set[7] in 2D, and the origin $O = [0\ 0]^{\mathrm{T}} \notin \bar{\Omega}$. For any $\mathbf{s} \in \Omega$, the line segment connecting $\mathbf{s}$ and the origin will intersect $\partial\Omega$ at one or multiple points. Let $\mathbf{s}^\ddagger \in \partial\Omega$ denotes the closest intersection to the origin (see Fig. 2), then $f_0(\mathbf{s}^\ddagger) \le f_0(\mathbf{s})$.

Proof: Based on the construction of $\mathbf{s}^\ddagger$, we have $\mathbf{s}^\ddagger = \varkappa\mathbf{s}$, with $\varkappa \in (0,1)$, and thus:

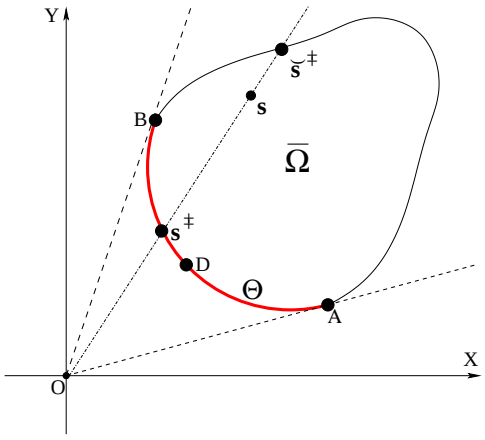

Fig. 2. Geometric illustration of Lemma 3. The global optimal solution resides only in Θ, i.e., the portion of the boundary of the feasible set $\bar{\Omega}$ (depicted by the red-colored curve ADB), defined by the two tangent lines OA and OB, which is closest to O.

$$\frac{(\mathbf{s}^\ddagger)(\mathbf{s}^\ddagger)^{\mathrm{T}}}{(\mathbf{s}^\ddagger)^{\mathrm{T}}(\mathbf{s}^\ddagger)} = \frac{\mathbf{s}\mathbf{s}^{\mathrm{T}}}{\mathbf{s}^{\mathrm{T}}\mathbf{s}}\ ,\ \frac{\mathbf{J}(\mathbf{s}^\ddagger)(\mathbf{s}^\ddagger)^{\mathrm{T}}\mathbf{J}^{\mathrm{T}}}{((\mathbf{s}^\ddagger)^{\mathrm{T}}(\mathbf{s}^\ddagger))^2} = \frac{1}{\varkappa^2}\frac{\mathbf{J}\mathbf{s}\mathbf{s}^{\mathrm{T}}\mathbf{J}^{\mathrm{T}}}{(\mathbf{s}^{\mathrm{T}}\mathbf{s})^2} \succeq \frac{\mathbf{J}\mathbf{s}\mathbf{s}^{\mathrm{T}}\mathbf{J}^{\mathrm{T}}}{(\mathbf{s}^{\mathrm{T}}\mathbf{s})^2}$$

$$\Rightarrow \quad \left(\mathbf{\Lambda} + \frac{\kappa_d}{\sigma_d^2}\frac{(\mathbf{s}^\ddagger)(\mathbf{s}^\ddagger)^{\mathrm{T}}}{(\mathbf{s}^\ddagger)^{\mathrm{T}}(\mathbf{s}^\ddagger)} + \frac{\kappa_\theta}{\sigma_\theta^2}\frac{\mathbf{J}(\mathbf{s}^\ddagger)(\mathbf{s}^\ddagger)^{\mathrm{T}}\mathbf{J}^{\mathrm{T}}}{((\mathbf{s}^\ddagger)^{\mathrm{T}}(\mathbf{s}^\ddagger))^2}\right)^{-1}$$

$$\preceq \left(\mathbf{\Lambda} + \frac{\kappa_d}{\sigma_d^2}\frac{\mathbf{s}\mathbf{s}^{\mathrm{T}}}{\mathbf{s}^{\mathrm{T}}\mathbf{s}} + \frac{\kappa_\theta}{\sigma_\theta^2}\frac{\mathbf{J}\mathbf{s}\mathbf{s}^{\mathrm{T}}\mathbf{J}^{\mathrm{T}}}{(\mathbf{s}^{\mathrm{T}}\mathbf{s})^2}\right)^{-1} \quad \Rightarrow \quad f_0(\mathbf{s}^\ddagger) \le f_0(\mathbf{s})$$

■

Remark 5: Lemma 3 establishes the fact that the global optimal solution for Π_3, when optimizing over the feasible set $\bar{\Omega}$ (see Fig. 2), is always on its *boundary* $\partial\Omega$, defined by (33)-(34), i.e., $\mathbf{s}^*$ satisfies either $\|\mathbf{s}^*-\mathbf{c}\| = r$ or $\|\mathbf{s}^*\| = \rho$. Moreover, by applying the same argument as before (see Fig. 2), it can be easily shown that $f_0(\mathbf{s}^\ddagger) \le f_0(\breve{\mathbf{s}}^\ddagger)$, where $\breve{\mathbf{s}}^\ddagger$ is any other intersection point in the direction of $\mathbf{s}^\ddagger$. Therefore, the global optimal solution $\mathbf{s}^*$ resides only in the portion of $\partial\Omega$ facing the origin, denoted as Θ (see Fig. 2)[8].

As shown in Figs. 3(a)-3(d), depending on the values of the parameters $\mathbf{c}$, r, and ρ, there exist four cases that we need to consider for the feasible set $\bar{\Omega}$ of Π_3. In what follows, we *analytically* solve the KKT conditions (35)-(37) for each of the first three cases [see Figs. 3(a)-3(c)], while for the fourth case [see Fig. 3(d)], we propose a strategy for handling the empty (or infeasible) set $\bar{\Omega}$. In the ensuing derivations, we use the definitions $\mathbf{s}^* := [x\ y]^{\mathrm{T}}$ and $\mathbf{c} := [c_1\ c_2]^{\mathrm{T}}$.

A. Case I: $0 < \rho \le \|\mathbf{c}\| - r$

As shown in Fig. 3(a), the only *active* constraint for Case I is the maximum-speed constraint [see (33)]. Based on Lemma 3 and setting $v = v_{\max}$, the optimal solution $\mathbf{s}^*$ must reside in the arc ADB, where A and B are two tangent points, whose Cartesian coordinates are computed later on [see (53)]. Since the collision-avoidance constraint (34) is *inactive*, its

[6] To simplify notation, we drop the indices of $\mathbf{s}_1$, σ_{d_1}, σ_{θ_1}, κ_{d_1}, κ_{θ_1}, $\mathbf{c}_1$, r_1, and ρ_1.

[7] Ω stands for the open set consisting of all interior points of $\bar{\Omega}$, while $\partial\Omega$ and $\bar{\Omega}$ represent its boundary and closure, respectively.

[8] It is straightforward to extend and generalize Lemma 3 to the multi-sensor case and conclude that the global optimal solution $\{\mathbf{s}_i^*, i = 1,\ldots,M\}$ for Π_2 is also always on the *boundary* of the feasible sets defined by (30)-(31), i.e., $\mathbf{s}_i^*$ satisfies either $\|\mathbf{s}_i^* - \mathbf{c}_i\| = r_i$ or $\|\mathbf{s}_i^*\| = \rho_i, \forall i = 1,\ldots,M$.

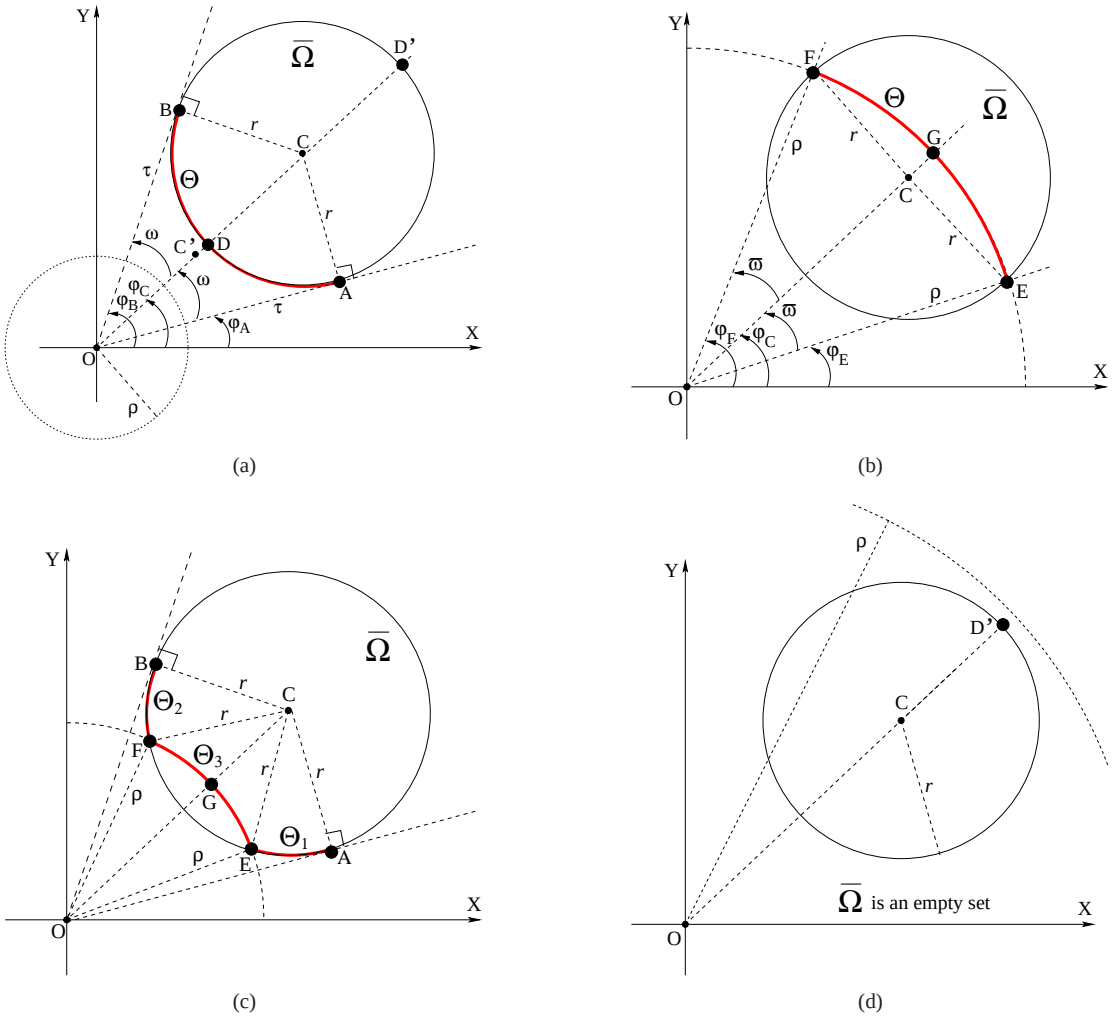

Fig. 3. Four cases of the feasible set $\bar{\Omega}$. (a) Case I: $0 < \rho \leq \|\mathbf{c}\| - r$. (b) Case II: $\sqrt{\|\mathbf{c}\|^2 - r^2} \leq \rho < \|\mathbf{c}\| + r$. (c) Case III: $\|\mathbf{c}\| - r < \rho < \sqrt{\|\mathbf{c}\|^2 - r^2}$. (d) Case IV: $\|\mathbf{c}\| + r \leq \rho$, which corresponds to the feasible set $\bar{\Omega}$ being empty. In the first three cases (a)-(c), the global optimal solution resides in a subset Θ of the boundary of $\bar{\Omega}$, which is depicted by the red-colored curve ADB in Case I, EGF in Case II, $AEGFB$ in Case III, respectively. In the above plots, O is the origin; C is the center of the circle $\|\mathbf{s} - \mathbf{c}\| = r$; A and B are the two tangent points residing in the circle $\|\mathbf{s} - \mathbf{c}\| = r$; E and F are the intersection points of the two circles $\|\mathbf{s} - \mathbf{c}\| = r$ and $\|\mathbf{s}\| = \rho$; the ray starting from O and passing through C intersects the circle $\|\mathbf{s}\| = \rho$ at G, and the circle $\|\mathbf{s} - \mathbf{c}\| = r$ at D and D'. Finally C' is the midpoint between O and C.

corresponding Lagrange multiplier $\nu^* = 0$, and the system of (35)-(37) is simplified to:

$$\nabla f_0(\mathbf{s}^*) + \mu^* (\mathbf{s}^* - \mathbf{c}) = \mathbf{0}_{2\times 1} \tag{38}$$

$$\|\mathbf{s}^* - \mathbf{c}\|^2 - r^2 = 0 \tag{39}$$

Clearly, (39) is a 2nd-order polynomial equation in the variables x and y, i.e.,

$$0 = f_2(x, y) = (x - c_1)^2 + (y - c_2)^2 - r^2 \tag{40}$$

Since we aim at transforming (38) into a polynomial equation only containing x and y, we eliminate μ^* by multiplying both sides of (38) with $(\mathbf{s}^* - \mathbf{c})^{\mathrm{T}} \mathbf{C} \left(\frac{\pi}{2}\right)$, which yields:

$$(\mathbf{s}^* - \mathbf{c})^{\mathrm{T}} \mathbf{C} \left(\frac{\pi}{2}\right) \nabla f_0(\mathbf{s}^*) = 0 \tag{41}$$

Note that (41) is equivalent to the following bivariate polynomial equation (see Appendix C):

$$0 = f_1(x, y) = \beta_3 xy\Delta^3 + (\alpha_8 x + \alpha_7 y + \beta_2)xy\Delta^2 + (\alpha_6 x^3 + \alpha_5 x^2 y + \alpha_4 xy^2 + \alpha_3 y^3 + \beta_1 xy)\Delta + (\alpha_2 x + \alpha_1 y)xy \tag{42}$$

where $\Delta := x^2 + y^2$, and the parameters $\beta_i,\ i = 1, 2, 3$, and $\alpha_j,\ j = 1, \ldots, 8$, are known coefficients expressed in terms of $\lambda_1, \lambda_2, c_1, c_2, \kappa_d \sigma_d^{-2}$, and $\kappa_\theta \sigma_\theta^{-2}$.

In order to obtain all the critical points of Π_3, we need to solve the system of polynomial equations $f_1(x, y) = 0$ *and* $f_2(x, y) = 0$ analytically [see (40) and (42)]. Although $f_2(x, y)$ is independent of the measurement type, $f_1(x, y)$ is a function of κ_d and κ_θ. Additionally, as it will become evident, the total degree of $f_1(x, y)$ depends on $\lambda_1 - \lambda_2$. (Note that in Lemma 2 it is assumed that $\lambda_1 \geq \lambda_2$). In what follows, we first present the solution of the system of bivariate polynomial equations (40) and (42) under the assumption $\lambda_1 > \lambda_2$ for each different type of measurement (see Sections IV-A1-IV-A3), and then address the case of $\lambda_1 = \lambda_2$ (see Section IV-A4).

1) Distance-and-Bearing Observations: When the sensor measures both distance and bearing to the target, or equivalently, $\kappa_d = \kappa_\theta = 1$, it can be shown (see Appendix D) that

$\beta_i \neq 0, i = 1, 2, 3$, and $\alpha_j \neq 0, j = 1, \ldots, 8$. Therefore, f_1 [see (42)] is an 8th-order polynomial in the variables x and y.

To solve $f_1 = f_2 = 0$ analytically, we first treat x as a parameter and rewrite (42) as a sum of y-monomials in decreasing order:

$$f_1 = \chi_7 y^7 + \chi_6 y^6 + \chi_5 y^5 + \chi_4 y^4 + \chi_3 y^3 + \chi_2 y^2 + \chi_1 y + \chi_0 \quad (43)$$

where χ_i, $i = 0, \ldots, 7$, are coefficients expressed in terms of $\lambda_1, \lambda_2, c_1, c_2, \sigma_d^{-2}, \sigma_\theta^{-2}$, and x (see Appendix D for the specific expressions of χ_i, $i = 0, \ldots, 7$).

Similarly, (40) can be rewritten as:

$$f_2 = \eta_2 y^2 + \eta_1 y + \eta_0 \quad (44)$$

where

$$\eta_2 = 1, \quad \eta_1 = -2c_2, \quad \eta_0 = x^2 - 2c_1 x + c_1^2 + c_2^2 - r^2 \quad (45)$$

Thus, the Sylvester matrix of f_1 and f_2 with respect to y, denoted as $\mathbf{Syl}(f_1, f_2; y)$, is the following 9×9 matrix [28, Ch. 3]:

$$\mathbf{Syl}(f_1, f_2; y) = \begin{bmatrix} \chi_7 & & \eta_2 & & & & & & \\ \chi_6 & \chi_7 & \eta_1 & \eta_2 & & & & & \\ \chi_5 & \chi_6 & \eta_0 & \eta_1 & \eta_2 & & & & \\ \chi_4 & \chi_5 & & \eta_0 & \eta_1 & \eta_2 & & & \\ \chi_3 & \chi_4 & & & \eta_0 & \eta_1 & \eta_2 & & \\ \chi_2 & \chi_3 & & & & \eta_0 & \eta_1 & \eta_2 & \\ \chi_1 & \chi_2 & & & & & \eta_0 & \eta_1 & \eta_2 \\ \chi_0 & \chi_1 & & & & & & \eta_0 & \eta_1 \\ & \chi_0 & & & & & & & \eta_0 \end{bmatrix}$$

The resultant of f_1 and f_2 with respect to y, denoted as $\mathbf{Res}(f_1, f_2; y)$, is the determinant of the Sylvester matrix $\mathbf{Syl}(f_1, f_2; y)$. Furthermore, note that since χ_i, $i = 0, \ldots, 7$, and η_0 are polynomials of x, $\mathbf{Res}(f_1, f_2; y)$ is also a polynomial of x only. Hence, by employing the Sylvester resultant [28, Ch. 3], we are able to eliminate variable y from (43) and (44), and obtain the following 10th-order univariate polynomial in variable x:

$$0 = f_3(x) = \mathbf{Res}(f_1, f_2; y) := \det\big(\mathbf{Syl}(f_1, f_2; y)\big) = \sum_{j=0}^{10} \gamma_j x^j \quad (46)$$

where γ_j, $j = 0, \ldots, 10$, are known coefficients expressed in terms of $\lambda_1, \lambda_2, c_1, c_2, \sigma_d^{-2}, \sigma_\theta^{-2}$, and r.

The roots of the univariate polynomial f_3 correspond to the 10 eigenvalues of the associated 10×10 companion matrix $\mathbf{\Gamma}$ [29]:

$$\mathbf{\Gamma} = \begin{bmatrix} 0 & & & -\gamma_0/\gamma_{10} \\ 1 & 0 & & -\gamma_1/\gamma_{10} \\ & \ddots & & \vdots \\ & & 1 & -\gamma_9/\gamma_{10} \end{bmatrix}$$

Note also that we only need to consider the real solutions of (46). Once x is determined, y is computed from (40), which can have at most 2 real solutions for every real solution x. In addition, from Lemma 3, we only need to consider those critical points *belonging to* the arc ADB. Thus the set $\bar{\Xi}_1$ consisting of all critical points $\mathbf{s}^* = [x \ y]^{\mathrm{T}}$, has at most 20 elements.

The final step is to evaluate the objective function $f_0(\mathbf{s})$ [see (32)] at all the critical points in $\bar{\Xi}_1$ and select the one with the smallest objective value as the global optimal solution of Π_3, for the case $\kappa_d = \kappa_\theta = 1, \lambda_1 > \lambda_2$, and $\rho \leq \|\mathbf{c}\| - r$.

2) Bearing-Only Observation: When only a bearing measurement is available, i.e., $\kappa_d = 0, \kappa_\theta = 1$, it can be shown (see Appendix E) that $\beta_3 = \alpha_8 = \alpha_7 = 0$, and $\beta_2 > 0$. Thus, $f_1(x, y)$ [see (42)] can be simplified into the following 6th-order bivariate polynomial:

$$0 = f_1(x, y) = \beta_2 xy\Delta^2 + (\alpha_6 x^3 + \alpha_5 x^2 y + \alpha_4 x y^2 + \alpha_3 y^3 + \beta_1 xy)\Delta + (\alpha_2 x + \alpha_1 y)xy \quad (47)$$

Similarly to the case of distance-and-bearing observations, we rewrite f_1 as:

$$f_1 = \zeta_5 y^5 + \zeta_4 y^4 + \zeta_3 y^3 + \zeta_2 y^2 + \zeta_1 y + \zeta_0 \quad (48)$$

where ζ_i, $i = 0, \ldots, 5$, are coefficients expressed in terms of $\lambda_1, \lambda_2, c_1, c_2, \sigma_\theta^{-2}$, and x (see Appendix E).

The Sylvester matrix of f_1 and f_2 [see (40) and (48)] with respect to y is the following 7×7 matrix, where η_0, η_1, η_2 are defined in (45):

$$\mathbf{Syl}(f_1, f_2; y) = \begin{bmatrix} \zeta_5 & & \eta_2 & & & & \\ \zeta_4 & \zeta_5 & \eta_1 & \eta_2 & & & \\ \zeta_3 & \zeta_4 & \eta_0 & \eta_1 & \eta_2 & & \\ \zeta_2 & \zeta_3 & & \eta_0 & \eta_1 & \eta_2 & \\ \zeta_1 & \zeta_2 & & & \eta_0 & \eta_1 & \eta_2 \\ \zeta_0 & \zeta_1 & & & & \eta_0 & \eta_1 \\ & \zeta_0 & & & & & \eta_0 \end{bmatrix}$$

The resultant of f_1 and f_2 with respect to y is a 6th-order univariate polynomial:

$$0 = f_3(x) = \mathbf{Res}(f_1, f_2; y) := \det\big(\mathbf{Syl}(f_1, f_2; y)\big) = \sum_{j=0}^{6} \psi_j x^j \quad (49)$$

where ψ_j, $j = 0, \ldots, 6$, are known coefficients expressed in terms of $\lambda_1, \lambda_2, c_1, c_2, \sigma_\theta^{-2}$, and r. The real roots of f_3 are the real eigenvalues of the 6×6 companion matrix $\mathbf{\Psi}$:

$$\mathbf{\Psi} = \begin{bmatrix} 0 & & & -\psi_0/\psi_6 \\ 1 & 0 & & -\psi_1/\psi_6 \\ & \ddots & & \vdots \\ & & 1 & -\psi_5/\psi_6 \end{bmatrix}$$

Once x is determined, y can be computed from (40), and those pairs of $[x \ y]^{\mathrm{T}}$ falling on the arc ADB are included in the set $\bar{\Xi}_1$, which has at most 12 elements.

Finally we evaluate the objective function $f_0(\mathbf{s})$ [see (32)] at all the critical points in $\bar{\Xi}_1$ and select the one with the smallest objective value as the global optimal solution of Π_3, for the case $\kappa_d = 0, \kappa_\theta = 1, \lambda_1 > \lambda_2$, and $\rho \leq \|\mathbf{c}\| - r$.

3) Distance-Only Observation: When the sensor can only measure its distance to the target, i.e., $\kappa_d = 1, \kappa_\theta = 0$, it can be shown (see Appendix F) that the coefficients appearing in $f_1(x, y)$ [see (42)] are:

$$\beta_3 < 0, \quad \alpha_8 = -c_1\beta_3, \quad \alpha_7 = -c_2\beta_3$$
$$\beta_2 = \beta_1 = \alpha_6 = \alpha_5 = \alpha_4 = \alpha_3 = \alpha_2 = \alpha_1 = 0$$

Therefore, (42) can be simplified into the following 8th-order bivariate polynomial:

$$0 = f_1(x, y) = \beta_3 \Delta^2 xy(x^2 + y^2 - c_1 x - c_2 y) \quad (50)$$

Since $\Delta = x^2 + y^2 > 0$ and $\beta_3 < 0$, the roots of f_1 must

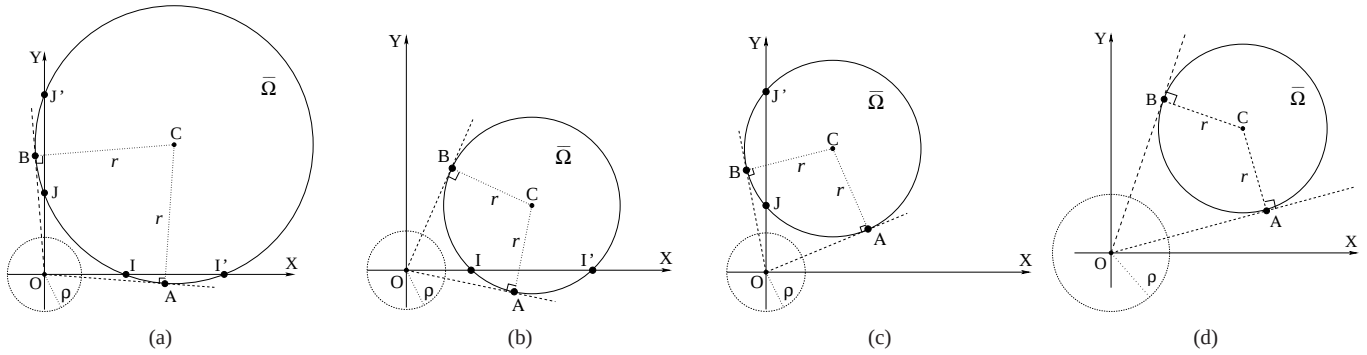

Fig. 4. Critical points for single-sensor target tracking with distance-only observations. (a) $\max(|c_1|,|c_2|) \leq r$: There exist six critical points, A,B,I,I',J,J'. (b) $|c_2| \leq r \leq |c_1|$: The four critical points are A,B,I,I'. (c) $|c_1| \leq r \leq |c_2|$: The four critical points are A,B,J,J'. (d) $\min(|c_1|,|c_2|) \geq r$: Only A and B are real critical points, and there exists no real solution satisfying $\xi_2(x,y)=0$ and $f_2(x,y)=0$ simultaneously.

satisfy *either* one of the following two polynomial equations:

$$0 = \xi_1(x,y) = x^2+y^2-c_1x-c_2y \tag{51}$$

$$0 = \xi_2(x,y) = xy \tag{52}$$

Thus, the set of all the critical points given a distance-only measurement is $\bar{\Xi}_{1l} \cup \bar{\Xi}_{1r}$, where $\bar{\Xi}_{1l} = \{(x,y)|\xi_1(x,y)=f_2(x,y)=0\}$ and $\bar{\Xi}_{1r} = \{(x,y)|\xi_2(x,y)=f_2(x,y)=0\}$. Note though that the set of possible global minima, $\bar{\Xi}_1$, contains only the critical points that belong to the arc ADB (see Lemma 3), and thus $\bar{\Xi}_1$ is a subset of $\bar{\Xi}_{1l} \cup \bar{\Xi}_{1r}$.

In order to determine the elements of $\bar{\Xi}_{1l}$, we note that (geometrically) ξ_1 [see (51)] and f_2 [see (40)] describe two circles in the plane whose intersection points belong to $\bar{\Xi}_{1l}$. In Appendix G, it is shown that $\bar{\Xi}_{1l}$ contains exactly two real elements, which correspond to the two tangent points A and B, shown in Fig. 3(a). The Cartesian coordinates of A and B are (see Appendix G):

$$\begin{bmatrix} x_A \\ y_A \end{bmatrix} = \tau \begin{bmatrix} \cos(\varphi_C - \omega) \\ \sin(\varphi_C - \omega) \end{bmatrix}, \quad \begin{bmatrix} x_B \\ y_B \end{bmatrix} = \tau \begin{bmatrix} \cos(\varphi_C + \omega) \\ \sin(\varphi_C + \omega) \end{bmatrix} \tag{53}$$

where [see Fig. 3(a)]

$$\tau = \sqrt{\|\mathbf{c}\|^2 - r^2},\ \varphi_C = \arctan\left(\frac{c_2}{c_1}\right),\ \omega = \arcsin\left(\frac{r}{\|\mathbf{c}\|}\right)$$

Next we focus on $\bar{\Xi}_{1r}$. It is straightforward to conclude from ξ_2 [see (52)] that *either* $x=0$ *or* $y=0$. Substituting $x=0$ or $y=0$ into $f_2=0$ [see (40)], we obtain the following four critical points [see Fig. 4(a)]:

$$[x_I\ y_I]^{\mathrm{T}} = \left[\mathrm{sign}(c_1)\left(|c_1| - \sqrt{r^2-c_2^2}\right) \quad 0\right]^{\mathrm{T}}, \text{if } |c_2| \leq r$$

$$[x_{I'}\ y_{I'}]^{\mathrm{T}} = \left[\mathrm{sign}(c_1)\left(|c_1| + \sqrt{r^2-c_2^2}\right) \quad 0\right]^{\mathrm{T}}, \text{if } |c_2| \leq r$$

$$[x_J\ y_J]^{\mathrm{T}} = \left[0 \quad \mathrm{sign}(c_2)\left(|c_2| - \sqrt{r^2-c_1^2}\right)\right]^{\mathrm{T}}, \text{if } |c_1| \leq r$$

$$[x_{J'}\ y_{J'}]^{\mathrm{T}} = \left[0 \quad \mathrm{sign}(c_2)\left(|c_2| + \sqrt{r^2-c_1^2}\right)\right]^{\mathrm{T}}, \text{if } |c_1| \leq r$$

where $\mathrm{sign}(x)$ is the sign function of a real variable x.

Note that the number of the real solutions satisfying $\xi_2 = f_2 = 0$ depends on $|c_1|, |c_2|$, and r. Specifically, if $\max(|c_1|,|c_2|) \leq r$ [see Fig. 4(a)], there are four real solutions (I, I', J, J') in $\bar{\Xi}_{1r}$. If $|c_2| \leq r \leq |c_1|$ [see Fig. 4(b)], $\bar{\Xi}_{1r}$ only consists of I and I'. Similarly, if $|c_1| \leq r \leq |c_2|$ [see Fig. 4(c)], only J and J' are valid solutions in $\bar{\Xi}_{1r}$. Finally, when $\min(|c_1|,|c_2|) \geq r$ [see Fig. 4(d)], $\bar{\Xi}_{1r}$ becomes an empty set, i.e., there exists no real solution that can fulfill $\xi_2=0$ and $f_2=0$ simultaneously.

In summary, $\bar{\Xi}_1$, containing all the critical points in the arc ADB, is a subset of $\bar{\Xi}_{1l} \cup \bar{\Xi}_{1r}$, which has at most six elements (A,B,I,I',J,J'). The final step is to evaluate the objective function $f_0(\mathbf{s})$ [see (32)] at all the critical points in $\bar{\Xi}_1$, and select the one with the smallest objective value as the global optimal solution of Π_3, for the case $\kappa_d = 1, \kappa_\theta = 0, \lambda_1 > \lambda_2$, and $\rho \leq \|\mathbf{c}\| - r$.

4) $\lambda_1 = \lambda_2 = \lambda$*:* In the previous sections, we have analyzed and presented the solutions for the three observation models under the assumption $\lambda_1 > \lambda_2$. We hereafter consider the special case $\lambda_1 = \lambda_2 = \lambda$, i.e., $\mathbf{\Lambda} = \lambda^{-1}\mathbf{I}_2$.

In Appendix H, we show that for single-sensor target tracking with bearing-only or distance-and-bearing observations, $f_1(x,y)$ [see (42)] can be transformed into a linear equation, $c_2x - c_1y = 0$, which depicts a line passing through the origin O and the center C [see Fig. 3(a)]. Furthermore, the coordinates $\mathbf{s}_D$ and $\mathbf{s}_{D'}$ of the two critical points D and D' (obtained by the intersection of the circle described by $f_2(x,y)=0$ [see (40)] with the line $f_1(x,y) = c_2x - c_1y = 0$), satisfy the relation $f_0(\mathbf{s}_D) \leq f_0(\mathbf{s}_{D'})$ (see Lemma 3). Therefore, for the bearing-only and distance-and-bearing observation models, the global optimal solution of Π_3 is $\mathbf{s}^* = \mathbf{s}_D = \frac{\mathbf{c}}{\|\mathbf{c}\|}\left(\|\mathbf{c}\| - r\right)$ [see Fig. 3(a)], when $\lambda_1 = \lambda_2$.

On the other hand, as shown in Appendix H, the objective function $f_0(\mathbf{s})$ in (32) remains a constant and is independent of $\mathbf{s}$ for single-sensor target tracking with distance-only measurements. In other words, $\nabla f_0(\mathbf{s}) = \mathbf{0}_{2\times 1}$ when $\kappa_d = 1, \kappa_\theta = 0, \lambda_1 = \lambda_2$. Thus, the sensor can move anywhere within $\bar{\Omega}$. However, in order to increase the probability of target re-detection at the following time steps, we require the sensor to move to D, which is the closest to the target point of $\bar{\Omega}$.

In summary, if $\lambda_1 = \lambda_2$, the best sensing location, regardless of the employed observation model, is D [see Fig. 3(a)], i.e.,

$\mathbf{s}^* = \mathbf{s}_D = \frac{\mathbf{c}}{\|\mathbf{c}\|}\big(\|\mathbf{c}\| - r\big)$.

B. Case II: $\sqrt{\|\mathbf{c}\|^2 - r^2} \le \rho < \|\mathbf{c}\| + r$

As shown in Fig. 3(b), and based on Lemma 3, the only *active* constraint for Case II is the collision-avoidance constraint (34), while the maximum-speed constraint (33) is *inactive* and hence its corresponding Lagrange multiplier is $\mu^* = 0$. Thus, (35)-(37) are simplified into:

$$\nabla f_0(\mathbf{s}^*) - \nu^* \mathbf{s}^* = \mathbf{0}_{2\times 1} \tag{54}$$

$$\|\mathbf{s}^*\|^2 - \rho^2 = 0 \tag{55}$$

Clearly, (55) is a 2nd-order polynomial equation in the variables x and y, i.e.,

$$0 = f_5(x, y) = x^2 + y^2 - \rho^2 \tag{56}$$

Applying the same technique as in Case I to eliminate ν^* from (54), yields:

$$(\mathbf{s}^*)^{\mathrm{T}} \mathbf{C} \left(\frac{\pi}{2}\right) \nabla f_0(\mathbf{s}^*) = 0 \tag{57}$$

Further analysis shows that, if (i) $\lambda_1 > \lambda_2$; *and* (ii) $\kappa_d \sigma_d^{-2} \rho^2 \neq \kappa_\theta \sigma_\theta^{-2}$ (which is automatically satisfied for the distance-only and bearing-only measurement models, and also holds true if $\rho \neq \frac{\sigma_d}{\sigma_\theta}$ for the distance-and-bearing observation model), then (57) is equivalent to the following 2nd-order bivariate polynomial f_4 (see Appendix I):

$$0 = f_4(x, y) = \; xy \tag{58}$$

It is easy to verify that the four real solutions satisfying f_4 [see (58)] and f_5 [see (56)] are $\big\{[\pm\rho \;\; 0]^{\mathrm{T}}, \; [0 \;\; \pm\rho]^{\mathrm{T}}\big\}$. However, *not all* these critical points belong to the feasible region $\bar{\Omega}$. In particular, $[-\mathrm{sign}(c_1)\rho \;\; 0]^{\mathrm{T}}$ and $[0 \;\; -\mathrm{sign}(c_2)\rho]^{\mathrm{T}}$ violate the maximum-speed constraint (33) (see Appendix K). The remaining two points $[\mathrm{sign}(c_1)\rho \;\; 0]^{\mathrm{T}}$ and $[0 \;\; \mathrm{sign}(c_2)\rho]^{\mathrm{T}}$ belong to $\bar{\Omega}$ [see Fig 3(b)], if the following conditions are satisfied (see Appendix K):

$$[\mathrm{sign}(c_1)\rho \;\; 0]^{\mathrm{T}} \in \bar{\Omega} \iff \big(\rho - |c_1|\big)^2 \le r^2 - c_2^2 \tag{59}$$

$$[0 \;\; \mathrm{sign}(c_2)\rho]^{\mathrm{T}} \in \bar{\Omega} \iff \big(\rho - |c_2|\big)^2 \le r^2 - c_1^2 \tag{60}$$

Hence, the set Ξ_2 containing all the *feasible* critical points has at most two elements. Specifically, if both (59) and (60) are satisfied, $\Xi_2 = \big\{[\mathrm{sign}(c_1)\rho \;\; 0]^{\mathrm{T}}, [0 \;\; \mathrm{sign}(c_2)\rho]^{\mathrm{T}}\big\}$; if only (59) is satisfied, $\Xi_2 = \big\{[\mathrm{sign}(c_1)\rho \;\; 0]^{\mathrm{T}}\big\}$; if only (60) is satisfied, $\Xi_2 = \big\{[0 \;\; \mathrm{sign}(c_2)\rho]^{\mathrm{T}}\big\}$; when neither (59) nor (60) is satisfied, $\Xi_2 = \varnothing$, which corresponds to the case shown in Fig. 3(b).

Since the curve EGF is an arc of the circle defined by (55), it is also necessary to consider the objective value attained at the two boundary points E and F, or equivalently, the intersection points of the two circles: $\|\mathbf{s} - \mathbf{c}\| = r$ and $\|\mathbf{s}\| = \rho$ [see Fig. 3(b)], whose Cartesian coordinates are (see Appendix L):

$$\begin{bmatrix} x_E \\ y_E \end{bmatrix} = \rho \begin{bmatrix} \cos(\varphi_C - \varpi) \\ \sin(\varphi_C - \varpi) \end{bmatrix}, \quad \begin{bmatrix} x_F \\ y_F \end{bmatrix} = \rho \begin{bmatrix} \cos(\varphi_C + \varpi) \\ \sin(\varphi_C + \varpi) \end{bmatrix} \tag{61}$$

where [see Fig. 3(b)]

$$\varphi_C = \arctan\left(\frac{c_2}{c_1}\right), \quad \varpi = \arccos\left(\frac{\rho^2 + \|\mathbf{c}\|^2 - r^2}{2\rho\|\mathbf{c}\|}\right)$$

Therefore, the set Ξ_2 is augmented into $\bar{\Xi}_2 = \Xi_2 \cup \{E, F\}$, which can have two, three, or at most four elements. The global optimal solution of Π_3 in Case II is selected as the $\mathbf{s}^* \in \bar{\Xi}_2$ with the smallest objective value $f_0(\mathbf{s}^*)$. Note that the sensor is not necessarily required to move at its maximum speed $v_{\max}$ in Case II.

Remark 6: The preceding derivations follow the assumption that (i) $\lambda_1 > \lambda_2$; *and* (ii) $\kappa_d \sigma_d^{-2} \rho^2 \neq \kappa_\theta \sigma_\theta^{-2}$. In Appendix J, we also address the special cases where (i) $\lambda_1 = \lambda_2$; or (ii) $\kappa_d = \kappa_\theta = 1$ and $\rho = \frac{\sigma_d}{\sigma_\theta}$, and show that $f_0(\mathbf{s})$ remains constant along the curve EGF [see Fig. 3(b)] if *either* one of these two conditions is satisfied. This means that any point belonging to the curve EGF is a *global optimal* solution. In such cases, we require the sensor to move to the location G [see Fig. 3(b)], which is the closest point of the arc EGF to C, i.e., $\mathbf{s}^* = \mathbf{s}_G = \frac{\mathbf{c}}{\|\mathbf{c}\|}\rho$.

C. Case III: $\|\mathbf{c}\| - r < \rho < \sqrt{\|\mathbf{c}\|^2 - r^2}$

As shown in Fig. 3(c), and based on Lemma 3, the optimal solution $\mathbf{s}^* \in \bar{\Omega}$ must reside on the curve $AEGFB$, which is composed of three segments, i.e., $\Theta = \Theta_1 \cup \Theta_2 \cup \Theta_3$. Θ_1 and Θ_2 are due to the maximum-speed constraint (33), and Θ_3 is due to the collision-avoidance constraint (34).

To obtain the critical points for Case III, we proceed as follows: We first ignore the collision-avoidance constraint (34), and calculate all critical points of Π_3 under the maximum-speed constraint (33) following the same process as for Case I (see Section IV-A). Note, however, that we only need to consider those critical points that reside in Θ_1 and Θ_2, which is a *subset* Ξ_3 of $\bar{\Xi}_1$. Then, we ignore the maximum-speed constraint (33) and apply the same method as for Case II (see Section IV-B) to compute the optimal solution $\mathbf{s}^\dagger$ of Π_3 over the set Θ_3. Following the above strategy, the set $\bar{\Xi}_3$ of all the critical points for Case III is $\bar{\Xi}_3 = \Xi_3 \cup \{\mathbf{s}^\dagger\}$.

The final step is to evaluate the objective function $f_0(\mathbf{s})$ at all the critical points in $\bar{\Xi}_3$, and select the one with the smallest objective value as the global optimal solution of Π_3.

D. Case IV: $\|\mathbf{c}\| + r \le \rho$

From the geometry of Fig. 3(d), we immediately conclude that there exists no real solution that satisfies both (33) and (34) simultaneously, i.e., the feasible set $\bar{\Omega}$ for Π_3 is empty. In this case, regardless of the measurement model, we require the sensor to move to D', as shown in Fig. 3(d), which ensures that (i) the sensor maintains the largest possible distance from the target so as to avoid collision, and (ii) it satisfies the maximum-speed constraint (33). Thus, the solution of Π_3 in Case IV is [see Fig. 3(d)]:

$$\mathbf{s}^* = \mathbf{s}_{D'} = \frac{\mathbf{c}}{\|\mathbf{c}\|}\big(r + \|\mathbf{c}\|\big)$$

E. Extension to Obstacle Avoidance and Additional Kinematic Constraints

Our approach to determine the global optimal solution for single-sensor target tracking, as described above, can be readily extended to include more complicated motion constraints, such as limitations on the sensor's kinematics and constraints imposed by obstacles. To proceed, we can employ one or multiple polynomials to describe (exactly or approximately) the obstacles' boundaries[9], or simply seek the minimal circle that encloses the obstacles. From Lemma 3, the global optimal solution must be on the boundary of the feasible set. In other words, if the obstacle-avoidance constraint is *active* and its associated Lagrange multiplier is *nonzero*, the global optimal solution must satisfy the polynomial equation describing the boundary of the obstacles, denoted as[10] $c(\mathbf{s}^*)=0$. Thus, the corresponding KKT necessary condition, similar to (38), has the form:[11]

$$\nabla f_0(\mathbf{s}^*)+\upsilon^*\nabla c(\mathbf{s}^*)=\mathbf{0}_{2\times 1} \tag{62}$$

where υ^* is the Lagrange multiplier. Moreover, since $c(\mathbf{s}^*)$ is a polynomial, $\nabla c(\mathbf{s}^*)$ is a 2×1 vector whose components are also polynomials in $\mathbf{s}^*$. To eliminate υ^*, we multiply both sides of (62) by $\left(\nabla c(\mathbf{s}^*)\right)^{\mathrm{T}}\mathbf{C}(\frac{\pi}{2})$, which yields:

$$\left(\nabla c(\mathbf{s}^*)\right)^{\mathrm{T}}\mathbf{C}\left(\frac{\pi}{2}\right)\nabla f_0(\mathbf{s}^*)=0 \tag{63}$$

Note that the only difference between (63) and (41) is that it contains the term $\nabla c(\mathbf{s}^*)$ instead of $\mathbf{s}^*-\mathbf{c}$. Therefore, we can apply the same process described in Section IV-A to transform (63) into a polynomial equation $f(x,y)=0$, and solve the corresponding polynomial system $f(x,y)=c(x,y)=0$ by employing the Sylvester resultant and the companion matrix. In fact, our approach can be generalized to solve any optimization problem with two optimization variables (i.e., 2D sensor motion), while only requiring that the objective function and all constraints are expressed as rational functions with respect to the two variables.

[9]Note that kinematic constraints can also be described as obstacles in the sensor's vicinity limiting its motion range.

[10]Since there exists a linear relation between $\mathbf{s}$ and $\mathbf{p}$ (see Lemma 2), any polynomial $h(\mathbf{p})$, expressed in $\mathbf{p}$, preserves its polynomial property under linear transformation, i.e., $h(\mathbf{p})=h\left(\mathbf{C}(\varphi_0)\,\mathbf{s}\right)=c(\mathbf{s})$, and $c(\mathbf{s})$ is a polynomial with respect to $\mathbf{s}$.

[11]Note that in (62) we only consider one constraint $c(\mathbf{s}^*)=c(x,y)=0$ as being active. In case of two (or more) *active* constraints $c_i(x,y)$ and $c_j(x,y)$, the solutions that simultaneously satisfy $c_i(x,y)=c_j(x,y)=0$ are generally discrete and finite. Thus, the optimal solution can be easily obtained by evaluating $f_0(\mathbf{s})$ at each solution and selecting the one with the smallest objective value.

V. Multiple-sensor Active Target Tracking: Gauss-Seidel Relaxation

Motivated by the simplicity of the analytic-form solution for the single-sensor optimal target tracking (see Section IV), a straightforward approach to solve the optimization problem Π_2 is to iteratively minimize its objective function [see (29)] for each optimization variable separately. Specifically, the solution of Π_2 is acquired by employing the cyclic coordinate descent method, also referred to as nonlinear Gauss-Seidel algorithm [30, Ch. 3], which requires to solve the following optimization problem at each step:

- Optimization Problem 4 (Π_4)

$$\begin{aligned}\min_{\mathbf{s}_i^{(\ell+1)}}\ \mathrm{tr}\Bigg(&\left(\mathbf{P}_i^{(\ell+1)}\right)^{-1}+\frac{\kappa_{d_i}}{\sigma_{d_i}^2}\frac{\left(\mathbf{s}_i^{(\ell+1)}\right)\left(\mathbf{s}_i^{(\ell+1)}\right)^{\mathrm{T}}}{\left(\mathbf{s}_i^{(\ell+1)}\right)^{\mathrm{T}}\left(\mathbf{s}_i^{(\ell+1)}\right)}\\&+\frac{\kappa_{\theta_i}}{\sigma_{\theta_i}^2}\frac{\mathbf{J}\left(\mathbf{s}_i^{(\ell+1)}\right)\left(\mathbf{s}_i^{(\ell+1)}\right)^{\mathrm{T}}\mathbf{J}^{\mathrm{T}}}{\left(\left(\mathbf{s}_i^{(\ell+1)}\right)^{\mathrm{T}}\left(\mathbf{s}_i^{(\ell+1)}\right)\right)^2}\Bigg)^{-1}\\ \text{s.t. }&\left\|\mathbf{s}_i^{(\ell+1)}-\mathbf{c}_i\right\|\le r_i\quad\text{and}\quad\left\|\mathbf{s}_i^{(\ell+1)}\right\|\ge\rho_i\end{aligned} \tag{64}$$

where $\mathbf{s}_i^{(\ell+1)}$ is the sought new optimal value of $\mathbf{s}_i$ at iteration $\ell+1$, $\mathbf{P}_i^{(\ell+1)}$ is defined in (65), and $\mathbf{s}_j^{(\ell+1)}, j=1,\ldots,i-1$, and $\mathbf{s}_j^{(\ell)}, j=i+1,\ldots,M$, are the remaining optimization variables, considered fixed during this step, computed sequentially during the previous iterations. Note that the matrix $\mathbf{P}_i^{(\ell+1)}$ is positive definite, and in general, non-diagonal. However, based on Lemma 2, through a similarity transformation, the optimization algorithm employed for a single sensor can be readily applied to solve Π_4.

The optimization process in the above Gauss-Seidel relaxation (GSR) algorithm (*sequentially* optimizing over $\mathbf{s}_1,\mathbf{s}_2,\ldots,\mathbf{s}_M$) is repeated until the maximum allowed number of iterations is reached (here set to 4), or the change in the objective function [see (29)] is less than 1%, whichever occurs first. Note that since the optimization process in the GSR algorithm is carried out sequentially for each variable $\mathbf{s}_i$, its computational complexity is only *linear* in the number of sensors, i.e., $\mathcal{O}(M)$. Furthermore, it is easily implemented, has low memory requirements and, as demonstrated in Section VI, it achieves the same level of tracking accuracy as the exhaustive search approach.

VI. Simulation Results

In order to evaluate the presented *constrained* optimal motion strategy, Gauss-Seidel Relaxation (GSR), we have conducted extensive simulation experiments and compared the performance of GSR to the following methods:

$$\left(\mathbf{P}_i^{(\ell+1)}\right)^{-1}=\mathbf{\Lambda}+\sum_{j=i+1}^{M}\left(\frac{\kappa_{d_j}}{\sigma_{d_j}^2}\frac{\left(\mathbf{s}_j^{(\ell)}\right)\left(\mathbf{s}_j^{(\ell)}\right)^{\mathrm{T}}}{\left(\mathbf{s}_j^{(\ell)}\right)^{\mathrm{T}}\left(\mathbf{s}_j^{(\ell)}\right)}+\frac{\kappa_{\theta_j}}{\sigma_{\theta_j}^2}\frac{\mathbf{J}\left(\mathbf{s}_j^{(\ell)}\right)\left(\mathbf{s}_j^{(\ell)}\right)^{\mathrm{T}}\mathbf{J}^{\mathrm{T}}}{\left(\left(\mathbf{s}_j^{(\ell)}\right)^{\mathrm{T}}\left(\mathbf{s}_j^{(\ell)}\right)\right)^2}\right)+\sum_{j=1}^{i-1}\left(\frac{\kappa_{d_j}}{\sigma_{d_j}^2}\frac{\left(\mathbf{s}_j^{(\ell+1)}\right)\left(\mathbf{s}_j^{(\ell+1)}\right)^{\mathrm{T}}}{\left(\mathbf{s}_j^{(\ell+1)}\right)^{\mathrm{T}}\left(\mathbf{s}_j^{(\ell+1)}\right)}+\frac{\kappa_{\theta_j}}{\sigma_{\theta_j}^2}\frac{\mathbf{J}\left(\mathbf{s}_j^{(\ell+1)}\right)\left(\mathbf{s}_j^{(\ell+1)}\right)^{\mathrm{T}}\mathbf{J}^{\mathrm{T}}}{\left(\left(\mathbf{s}_j^{(\ell+1)}\right)^{\mathrm{T}}\left(\mathbf{s}_j^{(\ell+1)}\right)\right)^2}\right) \tag{65}$$

• *Grid-Based Exhaustive Search* (GBES). In this case, we discretize the feasible set of all sensors and perform an exhaustive search over all possible combinations of these to find the one that minimizes the trace of the posterior covariance matrix for the target's position estimates [see (27)]. Ideally, the GBES should return the global optimal solution and it could be used as a benchmark for evaluating the GSR, if the grid size is sufficiently small. However, this is difficult to guarantee in practice since its computational complexity is exponential in the number of sensors. Hence implementing the GBES becomes prohibitive when the number of sensors, M, increases and/or when the size of the grid cells decreases. Throughout the simulations, we discretize the curve Θ [see Figs. 3(a)–3(c)] for each sensor-i ($i = 1, \ldots, M$) into 24 cells (arcs) of equal length.

• *Gradient Descent with Constant Step Size* (GDC). In order to compare GSR with the methods proposed in [13] and [23], we implemented the steepest-descent algorithm [27, Ch. 1] with the same step size $\alpha = 50$ as in [13]. However, both [13] and [23] do not address the sensors' motion constraints. Therefore, to account for mobility constraints, we project each solution $\mathbf{s}_i^*$ generated by GDC back into the sensor-i's feasible region $\bar{\Omega}_i$, if $\mathbf{s}_i^* \notin \bar{\Omega}_i$ ($i = 1, \ldots, M$).

• *Random Motion* (RM). This is a modification of an intuitive strategy that would require the sensors to move towards the target. In this case, however, and in order to ensure that the sensors do not converge to the same point, we require that at every time step sensor-i ($i = 1, \ldots, M$) selects its heading direction with uniform probability towards points within the curve Θ [see Figs. 3(a)–3(c)].

A. Simulation Setup

For the purposes of this simulation, we adopt a zero-acceleration target motion model:

$$\dot{\mathbf{x}}_T(t) = \mathbf{F}\ \mathbf{x}_T(t) + \mathbf{G}\ \mathbf{w}(t) \tag{66}$$

where

$$\mathbf{F} = \begin{bmatrix} 0 & 0 & 1 & 0 \\ 0 & 0 & 0 & 1 \\ 0 & 0 & 0 & 0 \\ 0 & 0 & 0 & 0 \end{bmatrix}, \mathbf{G} = \begin{bmatrix} 0 & 0 \\ 0 & 0 \\ 1 & 0 \\ 0 & 1 \end{bmatrix}, \mathbf{x}_T(t) = \begin{bmatrix} x_T(t) \\ y_T(t) \\ \dot{x}_T(t) \\ \dot{y}_T(t) \end{bmatrix},$$

and $\mathbf{w}(t) = [w_x(t)\ w_y(t)]^{\mathrm{T}}$ is a zero-mean white Gaussian noise vector with covariance $\mathbb{E}\left[\mathbf{w}(t)\mathbf{w}^{\mathrm{T}}(t')\right] = q\mathbf{I}_2\delta(t-t')$, $q = 1$, and $\delta(t-t')$ is the Dirac delta. In our implementation, we discretize the continuous-time system model [see (66)] with time step $\delta t = 0.1$ sec.

The initial true state of the target is $\mathbf{x}_T(0) = [0, 0, -8, 6]^{\mathrm{T}}$. The initial estimate for the target's state is $\hat{\mathbf{x}}_T(0|0) = [2, -2, 0, 0]^{\mathrm{T}}$. This can be obtained by processing the first measurements from the sensors at time-step 0. At the beginning of the experiment, the sensors are randomly distributed within a circle of radius 5 m, which is at a distance of about 20 m from the target's initial position. The maximum speed for each sensor is set to 12 m/sec, i.e., the largest distance that a sensor can travel during any time step is 1.2 m. The minimum distance between the target and sensors is set to $\rho = 2$ m.

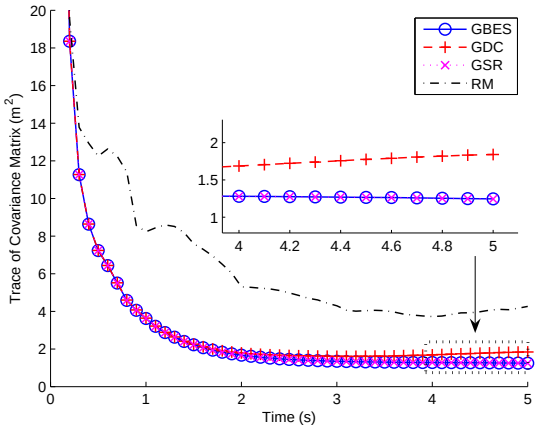

Fig. 5. [Two-sensor case] Trace of the target's position posterior covariance matrix. Comparison between GBES, GDC, GSR, and RM.

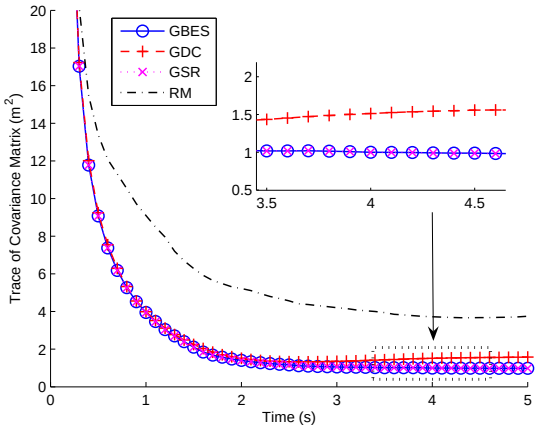

Fig. 6. [Two-sensor case, Monte Carlo simulations] Average trace of the target's position posterior covariance matrix in 50 experiments. Comparison between GBES, GDC, GSR, and RM.

The duration of the simulations is 5 sec (i.e., 50 time steps). At every time step, we employ the methods described (i.e., GBES, GDC, GSR, and RM) to calculate the next sensing location of each sensor.

B. Target Tracking with 2 Sensors (Homogeneous team)

We first investigate the scenario where 2 identical sensors track a moving target with distance-and-bearing observations (i.e., $\kappa_{d_i} = \kappa_{\theta_i} = 1,\ i = 1, 2$). The noise variances of the measurements are $\mathbf{R}_i = \mathrm{diag}(\sigma_{d_i}^2, \sigma_{\theta_i}^2)$ with $\sigma_{d_i}^2 = 4\ \mathrm{m}^2$, and $\sigma_{\theta_i}^2 = 0.5\ \mathrm{rad}^2,\ i = 1, 2$.

The time evolution of the trace of the target's position covariance in a typical simulation is shown in Fig. 5. As expected, the performance of GSR and GBES is improved compared to the case of GDC, and is significantly better than that of the non-optimized case RM. Additionally, the uncertainty in the target's position estimates (trace of the covariance matrix) achieved by the proposed GSR motion strategy is indistinguishable of that of the GBES, at a cost linear, instead of exponential, in the number of sensors. These

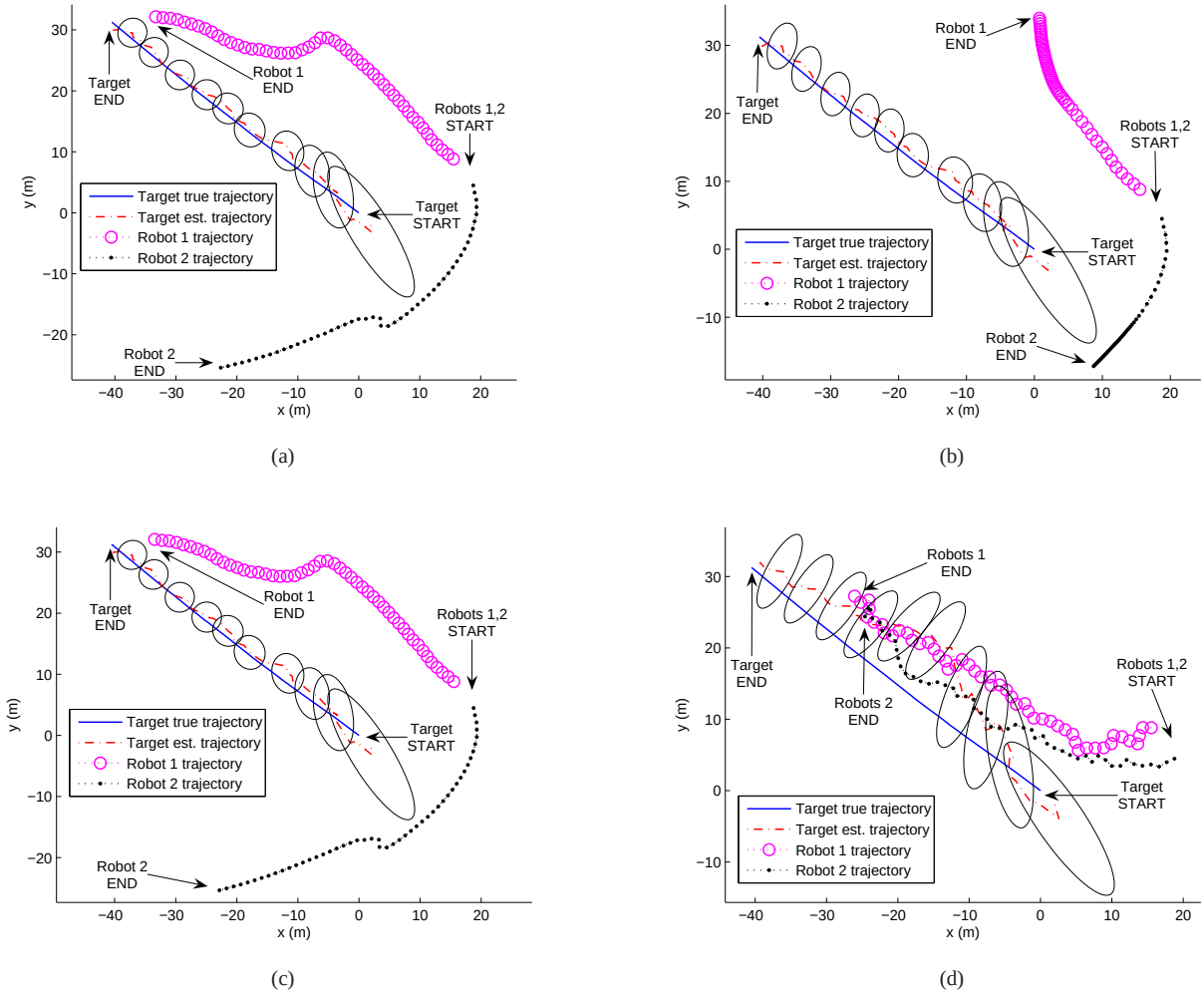

Fig. 7. [Two-sensor case] Trajectories of the two sensors, and the actual and estimated trajectories of the target, when employing as motion strategy (a) GBES, (b) GDC, (c) GSR, and (d) RM. The ellipses denote the 3σ bounds for the target's position uncertainty at the corresponding time steps.

results are typical for all experiments conducted and are summarized, for 50 trials, in Fig. 6.

Fig.s 7(a)–7(d) depict the actual and estimated trajectories of the target, along with the trajectories of the two sensors, when employing as motion strategy GBES, GDC, GSR, and RM, respectively. As evident, the accuracy of the target's position estimates for GSR is better than the case of GDC or RM, and almost identical to that of GBES. Additionally, the EKF produces consistent estimates for GSR, in other words, the real target's position is within the 3σ ellipse centered at the target's estimated position.

Finally, we plot the 2-norm of the estimation error between the true target position and its posterior estimate in Fig. 8, when employing as motion strategy GBES, GDC, GSR, and RM, respectively. As evident, the estimates produced by RM have the largest error. Note that the other three methods generate comparable estimation performance through most time steps, while GSR slightly outperforms GDC between the time interval 2 to 3 sec (i.e., time steps 20 to 30).

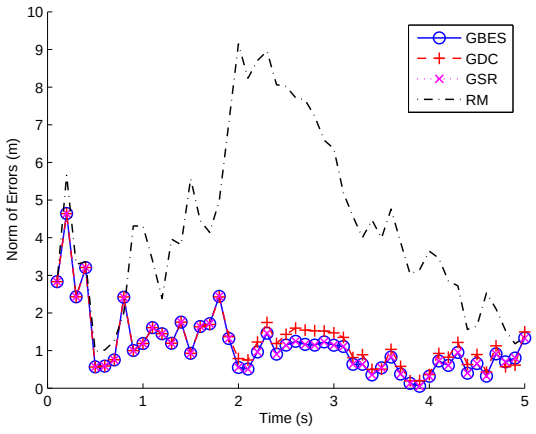

Fig. 8. [Two-sensor case] 2-norm of the actual error between the target's position estimate and its true value. Comparison between GBES, GDC, GSR, and RM.

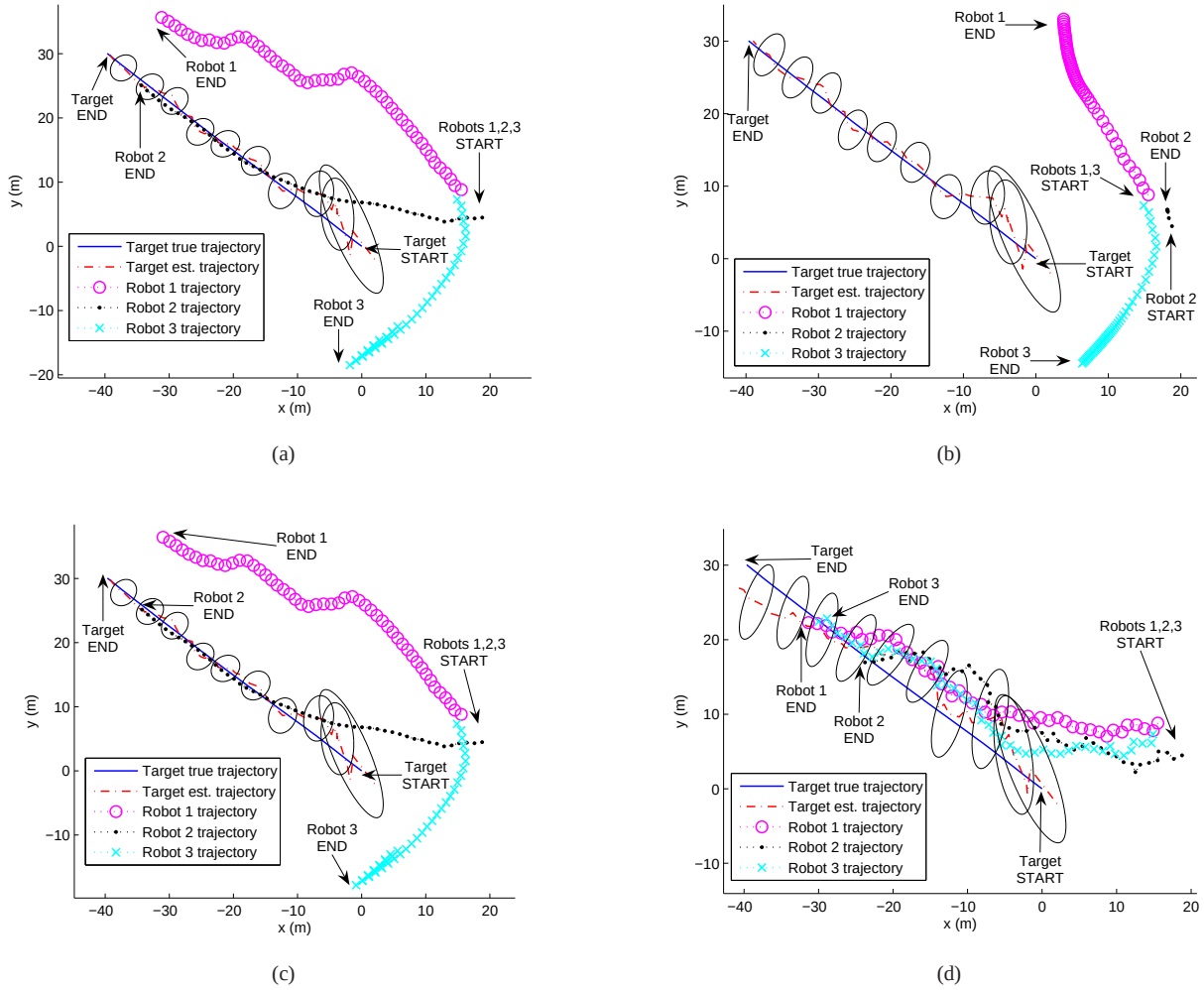

Fig. 10. [Three-sensor case] Trajectories of the three sensors, and the actual and estimated trajectories of the target, when employing as motion strategy (a) GBES, (b) GDC, (c) GSR, and (d) RM. The ellipses denote the 3σ bounds for the target's position uncertainty at the corresponding time steps.

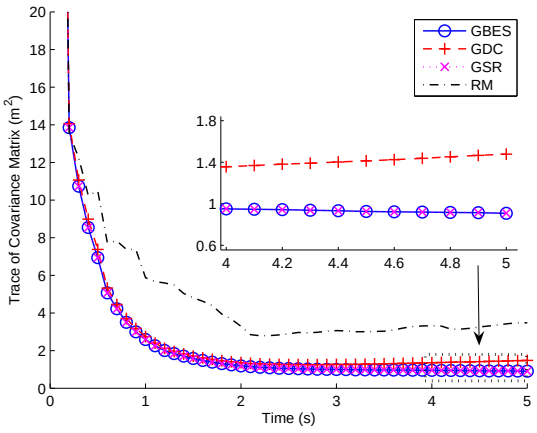

Fig. 9. [Three-sensor case] Trace of the target's position posterior covariance matrix. Comparison between GBES, GDC, GSR, and RM.

C. Target Tracking with 3 Sensors (Heterogeneous team)

We hereafter examine the performance of the GSR motion strategy for a heterogeneous team of 3 sensors tracking a moving target with a mixture of relative observations. In this case, sensor-1 can measure both distance and bearing to the target ($\kappa_{d_1} = \kappa_{\theta_1} = 1$), and its measurement noise covariance is set to $\mathbf{R}_1 = \text{diag}(\sigma^2_{d_1}, \sigma^2_{\theta_1})$ with $\sigma^2_{d_1} = 4$ m^2 and $\sigma^2_{\theta_1} = 0.5$ rad^2. On the other hand, sensor-2 can only record bearing observations ($\kappa_{d_2} = 0, \kappa_{\theta_2} = 1$) with measurement noise variance $\sigma^2_{\theta_2} = \sigma^2_{\theta_1}/2 = 0.25$ rad^2, while sensor-3 only has access to relative distance measurements ($\kappa_{d_3} = 1, \kappa_{\theta_3} = 0$) with noise variance $\sigma^2_{d_3} = \sigma^2_{d_1}/2 = 2$ m^2.

Fig.s 10(a)–10(d) depict the actual and estimated trajectories of the target, along with the trajectories of the three sensors, when employing as motion strategy GBES, GDC, GSR, and RM, respectively. As evident, the accuracy of the target's position estimates for GSR is better than that of GDC or RM, and almost identical to that of GBES. Furthermore, the EKF estimates for the sensors that employ the GSR motion strategy are consistent.

Interestingly, in this case for both the GBES and GSR motion strategies, sensor-2, which only measures relative bearing, immediately starts following the target, and attempts to minimize its distance to it. The reason for this is the

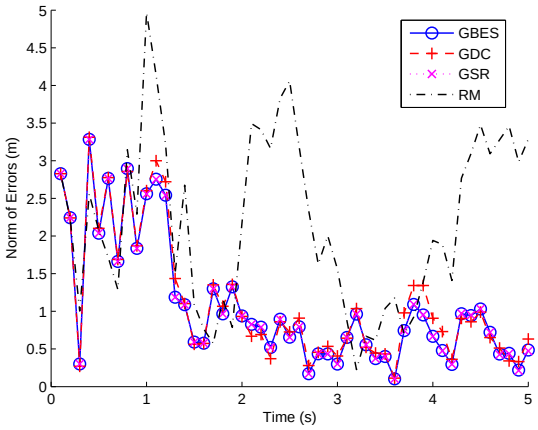

Fig. 11. [Three-sensor case] 2-norm of the actual error between the target's position estimate and its true value. Comparison between GBES, GDC, GSR, and RM.

following: As shown in Lemma 3, although the information contributed by a distance measurement (i.e., the term $\frac{1}{\sigma_d^2}\frac{\mathbf{s}\mathbf{s}^{\mathrm{T}}}{\mathbf{s}^{\mathrm{T}}\mathbf{s}}$ in the proof of Lemma 3) is independent of the relative distance $\|\mathbf{s}\|$ between the target and the sensor, the information from a bearing measurement (i.e., the term $\frac{1}{\sigma_\theta^2}\frac{\mathbf{J}\mathbf{s}\mathbf{s}^{\mathrm{T}}\mathbf{J}^{\mathrm{T}}}{(\mathbf{s}^{\mathrm{T}}\mathbf{s})^2}$ in the proof of Lemma 3) increases as the relative distance, $\|\mathbf{s}\|$, decreases. Therefore this prompts sensor-2 to approach the target as close as possible.

Finally, we note that the time evolution of the trace of the target's position covariance matrix is similar to that of the two-sensor case, and is illustrated in Fig. 9. Furthermore, the 2-norm of the estimation error is depicted in Fig. 11.

D. Scalability and Run-time

Contrary to the GBES method, which has computational and memory requirements exponential in the number of sensors, the complexity of the GSR algorithms is only linear. In order to corroborate our theoretical analysis, we have evaluated the computation time required by the four algorithms (GBES, GDC, GSR, and RM) for the case of a homogeneous sensor team ($\sigma_{d_i}^2 = 4$ m^2, and $\sigma_{\theta_i}^2 = 0.5$ rad^2, $i = 1, \ldots, M$) tracking a moving target. Specifically, we have examined the scalability of our algorithms by varying M from 2 to 100. These results are summarized in Table I. In contrast, due to its exponential computational complexity, we are only able to apply GBES to teams of up to 3 sensors.

Additionally, we plot the computational time with respect to the number of sensors in Fig. 12, when employing GSR as motion strategy. The plot clearly validates the claim that the GSR algorithm has linear, in the number of sensors, computational complexity. Finally, we should note that the main reason for the slower performance of the GSR algorithm (when compared to the GDC) is that we directly employ the MATLAB built-in function to compute the eigenvalues associated with the companion matrices, which improves the numerical accuracy at the expense of additional preprocessing steps. One of our future research direction is to improve the GSR performance (in terms of CPU running time) to be compared to that of the GDC.

TABLE I
COMPUTATIONAL TIME (SEC)

M	GBES	GDC	GSR	RM
2	0.1539	0.0002489	0.0011	0.00007053
3	8.9945	0.0002947	0.0014	0.00007106
10	N/A	0.0008	0.0047	0.0001263
20	N/A	0.0018	0.0109	0.0004553
30	N/A	0.0024	0.0153	0.0004853
40	N/A	0.0027	0.0185	0.0003653
50	N/A	0.0033	0.0227	0.0004121
60	N/A	0.0040	0.0274	0.0005056
70	N/A	0.0045	0.0315	0.0005477
80	N/A	0.0052	0.0362	0.0006736
90	N/A	0.0059	0.0406	0.0007331
100	N/A	0.0066	0.0450	0.0008845

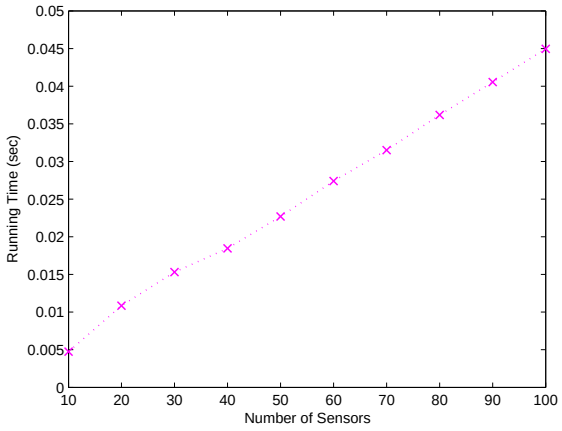

Fig. 12. CPU time vs. number of sensors, when employing GSR as motion strategy.

VII. EXPERIMENTAL RESULTS

We hereafter describe one of the experiments performed to validate the performance of our proposed GSR algorithm. Our experimental setup is shown in Fig. 13, where a team of three Pioneer II robots are deployed in a rectangular region of size approximately 4 m $\times$ 3 m. In Fig. 13, the target is shown at the bottom right, while the other two Pioneers are acting as tracking sensors. An overhead camera is employed to provide ground truth for evaluating the estimator's performance. To do so, rectangular boards with specific patterns (see Fig. 13) are mounted on top of the Pioneers, and the pose (position and orientation) of each Pioneer, with respect to a global frame of reference, is computed from the captured images.

In the experiment, we adopt a zero-acceleration target motion model, where the target moves with constant speed of approximately 0.1 m/sec. The process noise $\mathbf{w}(t)$ [see (66)] is assumed to be a zero-mean white Gaussian noise vector with covariance $\mathbb{E}\left[\mathbf{w}(t)\mathbf{w}^{\mathrm{T}}(t')\right] = 10^{-6}\mathbf{I}_2\delta(t-t')$. In our implementation, the sampling time is set to $\delta t = 0.5$ sec. The initial

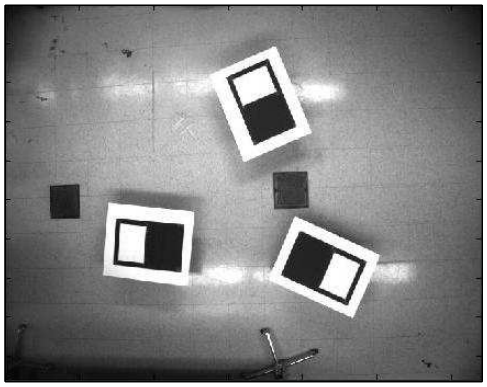

Fig. 13. [Two-sensor case, experimental setup] Three Pioneer robots, each with a pattern board attached on its top. The target is located at the bottom right of the image, while the other two robots act as tracking sensors.

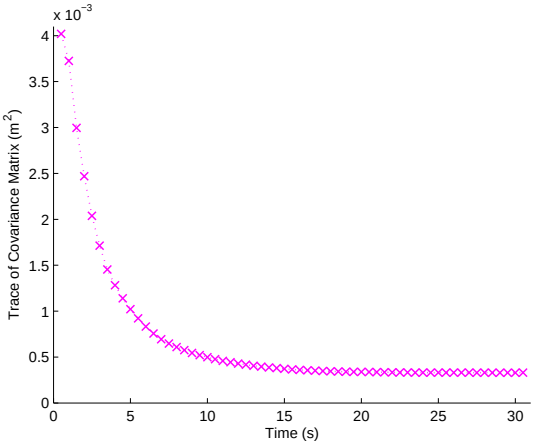

Fig. 14. [Two-sensor case, experimental result] Trace of the target's position posterior covariance matrix, when employing GSR as motion strategy.

true state of the target, computed from the overhead camera, is $\mathbf{x}_T(0) = [0.23, 0.16, 0.05, 0.01]^{\mathrm{T}}$, while the initial estimate for the target's state is set to $\hat{\mathbf{x}}_T(0|0) = [0, 0, 0, 0]^{\mathrm{T}}$. At the beginning, the two sensors are deployed at $\mathbf{p}_{S_1}(0) = [0.20, 1.69]^{\mathrm{T}}$ and $\mathbf{p}_{S_2}(0) = [2.34, 0.17]^{\mathrm{T}}$, respectively. The maximum speed for each sensor is set to 0.12 m/sec, and the minimum distance between the target and sensors is $\rho = 1$ m. We consider the scenario where each sensor measures both relative distance and bearing to the target (i.e., $\kappa_{d_i} = \kappa_{\theta_i} = 1$, $i = 1, 2$). These relative measurements are generated synthetically by adding noise to the relative distance and bearing calculated from the Pioneers' pose estimates using the overhead camera. In this experiment, the standard deviations of the distance and bearing measurement noise are set to $\sigma_{d_i} = 0.05$ m and $\sigma_{\theta_i} = 0.05$ rad, $i = 1, 2$, respectively.

The duration of the experiment is 30 sec (i.e., 60 time steps). At every time step, we employ the GSR method to calculate the next best sensing location of each sensor.

Fig. 14 depicts the time evolution of the trace of the target's position covariance, which shows that at steady state, the standard deviation of the estimation error along each direction is around 0.02 m. The real estimation error, computed as the 2-norm between the target's estimated and true position (obtained from the overhead camera), is shown in Fig. 15. As evident, the estimation error, when employing the GSR-based motion strategy, is immediately reduced from 0.28 m to 0.04 m, and is less than 0.05 m for most of the remaining time steps.

Fig. 16 depicts the actual and estimated trajectories of the target, along with the real trajectories of the two sensors, when employing the GSR-based motion strategy. Again, as was the case in the simulations, the EKF produces consistent estimates for GSR, i.e., the real target's position is within the 3σ ellipse centered at the target's estimated position. This validates that our proposed GSR algorithm is robust and applicable to real systems.

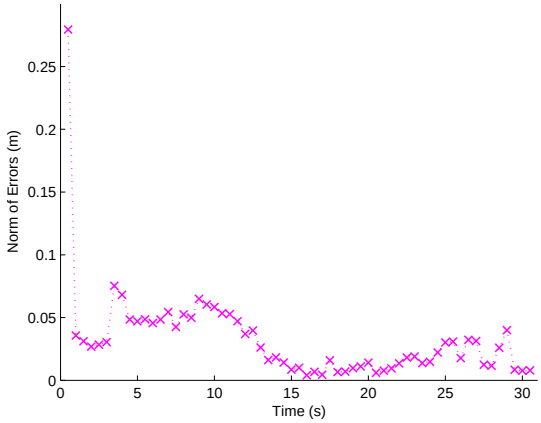

Fig. 15. [Two-sensor case, experimental result] 2-Norm of the error of the target's position posterior estimates, when employing GSR as motion strategy.

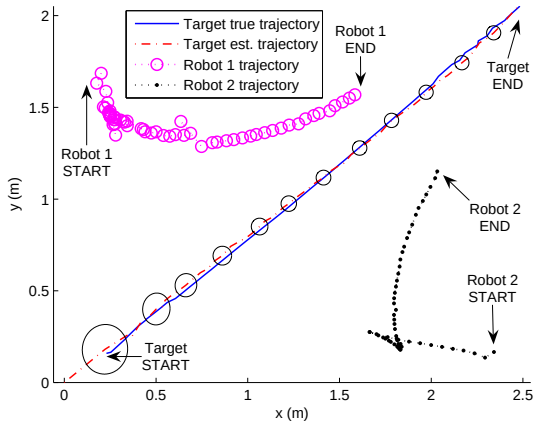

Fig. 16. [Two-sensor case, experimental result] Real trajectories of the two sensors, and the actual and estimated trajectories of the target, when employing GSR as motion strategy. The ellipses denote the 3σ bounds for the target's position uncertainty at the corresponding time steps.

VIII. Conclusions

In this paper, we have addressed the problem of *constrained* optimal motion strategies for *heterogeneous* teams of mobile sensors tracking a moving target using a *mixture* of relative observations (i.e., distance-only, bearing-only, or distance-and-bearing). In particular, our objective is to determine the best locations that the sensors should move to at every time step in order to collect the most informative measurements, i.e., the observations that minimize the trace of the target's position covariance matrix. In our formulation, we have explicitly considered motion constraints on the robots (maximum speed and minimum distance to the target), and we have shown that this non-convex constrained optimization problem is NP-Hard in general.

In order to derive a computationally efficient solution, we first investigated the optimal trajectory generation problem for single-sensor target tracking. Despite the fact that the constrained optimization problem is non-convex even for the single-sensor case, we derived its global optimal solution *analytically* by (i) transforming the associated KKT optimality conditions into a system of bivariate polynomial equations, and (ii) directly solving it using algebraic geometry methods. Furthermore, and in order to provide a real-time solution for the multi-sensor case, we leveraged the single-sensor result by relaxing the original NP-Hard problem. Specifically, we introduced an iterative algorithm, Gauss-Seidel relaxation (GSR), whose computational complexity is significantly lower compared to that of a grid-based exhaustive search (GBES) method (linear vs. exponential in the number of robots). Simulation studies show that the GSR algorithm achieves the same level of tracking accuracy as GBES, while it outperforms gradient-descent-based approaches. Furthermore, we performed experiments using a team of two mobile robots that demonstrate the applicability of the GSR algorithm to real systems.

In our future work, we plan to extend our current approach and address the cases when the robots' poses are uncertain and when multiple targets are present. Finally, we intend to investigate distributed implementations of the GSR algorithm that account for limitations on the sensors' communication bandwidth (by transmitting only quantized functions of their measurements [31], [6]) and range (by explicitly considering the time-varying communication topology when designing the estimator [32], [33]).

Appendix A
Proof of Lemma 1

Proof: The covariance matrices appearing in (20) are defined based on the following partition:

$$\mathbf{P}_{\ell|j} = \begin{bmatrix} \mathbf{P}_{\ell|j,11} & \mathbf{P}_{\ell|j,12} \\ \mathbf{P}_{\ell|j,12}^{\mathrm{T}} & \mathbf{P}_{\ell|j,22} \end{bmatrix} \tag{67}$$

where the 2×2 matrix $\mathbf{P}_{\ell|j,11}$ denotes the covariance for the target's *position* estimate, $\hat{\mathbf{p}}_T = [\hat{x}_T\ \hat{y}_T]^{\mathrm{T}}$, at time-step ℓ given measurements up to time-step j.

Employing the matrix inversion lemma [34], the covariance update equation (19) can be written as:

$$\mathbf{P}_{k+1|k+1}^{-1} = \mathbf{P}_{k+1|k}^{-1} + \mathbf{H}_{k+1}^{\mathrm{T}}\mathbf{R}^{-1}\mathbf{H}_{k+1} \tag{68}$$

Note that if the state vector only contains the position of the target, then (20) is identical to (68).

In the general case, when the state vector also contains higher-order derivatives of the position (e.g., velocity, acceleration, etc.), substituting

$$\mathbf{P}_{k+1|k}^{-1} = \boldsymbol{\Upsilon} = \begin{bmatrix} \boldsymbol{\Upsilon}_{11} & \boldsymbol{\Upsilon}_{12} \\ \boldsymbol{\Upsilon}_{12}^{\mathrm{T}} & \boldsymbol{\Upsilon}_{22} \end{bmatrix} \tag{69}$$

and

$$\mathbf{H}_{k+1}^{\mathrm{T}}\mathbf{R}^{-1}\mathbf{H}_{k+1} = \begin{bmatrix} \mathbf{H}_{e,k+1}^{\mathrm{T}}\mathbf{R}^{-1}\mathbf{H}_{e,k+1} & \mathbf{0}_{2\times(2N-2)} \\ \mathbf{0}_{(2N-2)\times 2} & \mathbf{0}_{(2N-2)\times(2N-2)} \end{bmatrix}$$

on the right hand-side of (68) yields:

$$\mathbf{P}_{k+1|k+1} = \begin{bmatrix} \boldsymbol{\Upsilon}_{11} + \mathbf{H}_{e,k+1}^{\mathrm{T}}\mathbf{R}^{-1}\mathbf{H}_{e,k+1} & \boldsymbol{\Upsilon}_{12} \\ \boldsymbol{\Upsilon}_{12}^{\mathrm{T}} & \boldsymbol{\Upsilon}_{22} \end{bmatrix}^{-1} \tag{70}$$

Employing the property of the Schur complement [34] for the inversion of a partitioned matrix in (69)-(70), we obtain:

$$\begin{aligned} \mathbf{P}_{k+1|k+1,11} &= \left(\boldsymbol{\Upsilon}_{11} + \mathbf{H}_{e,k+1}^{\mathrm{T}}\mathbf{R}^{-1}\mathbf{H}_{e,k+1} - \boldsymbol{\Upsilon}_{12}\boldsymbol{\Upsilon}_{22}^{-1}\boldsymbol{\Upsilon}_{12}^{\mathrm{T}}\right)^{-1} \\ &= \left(\left(\mathbf{P}_{k+1|k,11}\right)^{-1} + \mathbf{H}_{e,k+1}^{\mathrm{T}}\mathbf{R}^{-1}\mathbf{H}_{e,k+1}\right)^{-1} \end{aligned}$$

■

Appendix B
Rational functions $f_0(\mathbf{s}^*)$ and $\nabla f_0(\mathbf{s}^*)$

We hereafter show that $f_0(\mathbf{s}^*)$ [see (32)] is a rational function in $\mathbf{s}^* = [x\ y]^{\mathrm{T}}$, i.e.,

$$f_0(\mathbf{s}^*) = \frac{h(\mathbf{s}^*)}{g(\mathbf{s}^*)} \tag{71}$$

where $h(\mathbf{s}^*)$ and $g(\mathbf{s}^*)$ are polynomials in x and y, and thus

$$\nabla f_0(\mathbf{s}^*) = \frac{g(\mathbf{s}^*)\nabla h(\mathbf{s}^*) - h(\mathbf{s}^*)\nabla g(\mathbf{s}^*)}{g^2(\mathbf{s}^*)} \tag{72}$$

is also a rational function in x and y.

To proceed, note that $f_0(\mathbf{s}^*) = \mathrm{tr}(\mathbf{M}^{-1})$ where

$$\mathbf{M} = \boldsymbol{\Lambda} + \frac{\kappa_d}{\sigma_d^2}\frac{(\mathbf{s}^*)(\mathbf{s}^*)^{\mathrm{T}}}{(\mathbf{s}^*)^{\mathrm{T}}(\mathbf{s}^*)} + \frac{\kappa_\theta}{\sigma_\theta^2}\frac{\mathbf{J}(\mathbf{s}^*)(\mathbf{s}^*)^{\mathrm{T}}\mathbf{J}^{\mathrm{T}}}{\left((\mathbf{s}^*)^{\mathrm{T}}(\mathbf{s}^*)\right)^2} \tag{73}$$

Moreover, $\mathrm{tr}(\mathbf{M}^{-1}) = \frac{\mathrm{tr}(\mathbf{M})\cdot\varepsilon}{\det(\mathbf{M})\cdot\varepsilon}$ holds true for any nonzero scalar ε and any invertible 2×2 matrix $\mathbf{M}$. By defining $\varepsilon = \lambda_1\lambda_2(x^2+y^2)^2 > 0$, we obtain [see (71) and (73)]:

$$\begin{aligned} \mathrm{tr}\,(\mathbf{M}) &= \lambda_1^{-1} + \lambda_2^{-1} + \kappa_d\sigma_d^{-2} + \kappa_\theta\sigma_\theta^{-2}(x^2+y^2)^{-1} \\ \det(\mathbf{M}) &= \lambda_1^{-1}\lambda_2^{-1} + \kappa_d\sigma_d^{-2}\kappa_\theta\sigma_\theta^{-2}(x^2+y^2)^{-1} \\ &\quad + \lambda_1^{-1}\left[\kappa_d\sigma_d^{-2}(x^2+y^2)^{-1}y^2 + \kappa_\theta\sigma_\theta^{-2}(x^2+y^2)^{-2}x^2\right] \\ &\quad + \lambda_2^{-1}\left[\kappa_d\sigma_d^{-2}(x^2+y^2)^{-1}x^2 + \kappa_\theta\sigma_\theta^{-2}(x^2+y^2)^{-2}y^2\right] \\ h(\mathbf{s}^*) &= \mathrm{tr}\,(\mathbf{M})\cdot\varepsilon \\ &= a_2(x^2+y^2)^2 + a_1(x^2+y^2) \\ g(\mathbf{s}^*) &= \det(\mathbf{M})\cdot\varepsilon \\ &= b_6(x^2+y^2)^2 + b_5(x^2+y^2)x^2 + b_4(x^2+y^2)y^2 \\ &\quad + b_3(x^2+y^2) + b_2x^2 + b_1y^2 \end{aligned}$$

where the coefficients a_i $(i = 1, 2)$ and b_j $(j = 1, \ldots, 6)$ are expressed in terms of $\lambda_1, \lambda_2, \kappa_d\sigma_d^{-2}$, and $\kappa_\theta\sigma_\theta^{-2}$:

$$\begin{aligned} a_2 &= \lambda_1 + \lambda_2 + \lambda_1\lambda_2\kappa_d\sigma_d^{-2}, \quad a_1 = \lambda_1\lambda_2\kappa_\theta\sigma_\theta^{-2} \\ b_6 &= 1, \quad b_5 = \lambda_1\kappa_d\sigma_d^{-2}, \quad b_4 = \lambda_2\kappa_d\sigma_d^{-2} \\ b_3 &= \lambda_1\lambda_2\kappa_d\sigma_d^{-2}\kappa_\theta\sigma_\theta^{-2}, \quad b_2 = \lambda_2\kappa_\theta\sigma_\theta^{-2}, \quad b_1 = \lambda_1\kappa_\theta\sigma_\theta^{-2} \end{aligned} \tag{74}$$

and thus $f_0(\mathbf{s}^*) = \frac{h(\mathbf{s}^*)}{g(\mathbf{s}^*)}$ is a rational function in $\mathbf{s}^*$.

Since both $h(\mathbf{s}^*)$ and $g(\mathbf{s}^*)$ are bivariate polynomials, their derivatives $\nabla h(\mathbf{s}^*)$ and $\nabla g(\mathbf{s}^*)$ are 2×1 vectors with each component a bivariate polynomial. Specifically,

$$\nabla h(\mathbf{s}^*) = 2h_0(\mathbf{s}^*)\begin{bmatrix} x \\ y \end{bmatrix} \tag{75}$$

$$\nabla g(\mathbf{s}^*) = 2g_0(\mathbf{s}^*)\begin{bmatrix} x \\ y \end{bmatrix} + 2\begin{bmatrix} xg_x(\mathbf{s}^*) \\ yg_y(\mathbf{s}^*) \end{bmatrix} \tag{76}$$

where $h_0(\mathbf{s}^*), g_0(\mathbf{s}^*), g_x(\mathbf{s}^*)$, and $g_y(\mathbf{s}^*)$ are polynomials in x and y, defined as:

$$h_0(\mathbf{s}^*) = 2a_2(x^2 + y^2) + a_1 \tag{77}$$

$$g_0(\mathbf{s}^*) = 2b_6(x^2 + y^2) + b_5x^2 + b_4y^2 + b_3$$

$$g_x(\mathbf{s}^*) = b_5(x^2 + y^2) + b_2 \tag{78}$$

$$g_y(\mathbf{s}^*) = b_4(x^2 + y^2) + b_1 \tag{79}$$

Appendix C
Transforming (41) into (42)

By substituting the expressions of $\nabla f_0(\mathbf{s}^*)$, $\nabla h(\mathbf{s}^*)$, and $\nabla g(\mathbf{s}^*)$ [see (72)-(76)] into (41), and setting the numerator equal zero, we obtain the following polynomial equation with respect to x and y:

$$\begin{aligned} 0 = \; & x(y - c_2)\big[g(\mathbf{s}^*)h_0(\mathbf{s}^*) - h(\mathbf{s}^*)g_0(\mathbf{s}^*) - h(\mathbf{s}^*)g_x(\mathbf{s}^*)\big] \\ & - y(x - c_1)\big[g(\mathbf{s}^*)h_0(\mathbf{s}^*) - h(\mathbf{s}^*)g_0(\mathbf{s}^*) - h(\mathbf{s}^*)g_y(\mathbf{s}^*)\big] \end{aligned} \tag{80}$$

Rearranging terms in (80), yields:

$$\begin{aligned} 0 = \; & xyh(\mathbf{s}^*)\big[g_y(\mathbf{s}^*) - g_x(\mathbf{s}^*)\big] + h(\mathbf{s}^*)\big[c_2xg_x(\mathbf{s}^*) - c_1yg_y(\mathbf{s}^*)\big] \\ & + (c_1y - c_2x)\big[g(\mathbf{s}^*)h_0(\mathbf{s}^*) - h(\mathbf{s}^*)g_0(\mathbf{s}^*)\big] \end{aligned} \tag{81}$$

Substituting the expressions of $h(\mathbf{s}^*)$, $g(\mathbf{s}^*)$, $h_0(\mathbf{s}^*)$, $g_0(\mathbf{s}^*)$, $g_x(\mathbf{s}^*)$, $g_y(\mathbf{s}^*)$, and rearranging terms in (81), we obtain the polynomial equation (42):

$$\begin{aligned} 0 = f_1(x, y) = \; & \beta_3xy\Delta^3 + (\alpha_8x + \alpha_7y + \beta_2)xy\Delta^2 \\ & + (\alpha_6x^3 + \alpha_5x^2y + \alpha_4xy^2 + \alpha_3y^3 + \beta_1xy)\Delta + (\alpha_2x + \alpha_1y)xy \end{aligned}$$

where $\Delta := x^2 + y^2$, and

$$\begin{aligned} \beta_3 &= a_2(b_4 - b_5) \\ \beta_2 &= a_1(b_4 - b_5) + a_2(b_1 - b_2) \\ \beta_1 &= a_1(b_1 - b_2) \\ \alpha_8 &= c_1a_2(b_5 - b_4) \\ \alpha_7 &= c_2a_2(b_5 - b_4) \\ \alpha_6 &= c_2\left[a_1(b_5 + b_6) - a_2(b_2 + b_3)\right] \\ \alpha_5 &= c_1\left[a_2(b_3 + 2b_2 - b_1) - a_1(b_6 + b_4)\right] \\ \alpha_4 &= c_2\left[a_2(b_2 - 2b_1 - b_3) + a_1(b_6 + b_5)\right] \\ \alpha_3 &= c_1\left[a_2(b_3 + b_1) - a_1(b_6 + b_4)\right] \\ \alpha_2 &= c_1a_1(b_2 - b_1) \\ \alpha_1 &= c_2a_1(b_2 - b_1) \end{aligned} \tag{82}$$

Since $a_1, a_2, b_1, \ldots, b_6$ [see (74)] are coefficients expressed in terms of $\lambda_1, \lambda_2, \kappa_d\sigma_d^{-2}$, and $\kappa_\theta\sigma_\theta^{-2}$, thus from (82) we conclude that β_i, $i = 1, 2, 3$, and α_j, $j = 1, \ldots, 8$, are also functions of $\lambda_1, \lambda_2, c_1, c_2, \kappa_d\sigma_d^{-2}$, and $\kappa_\theta\sigma_\theta^{-2}$.

Appendix D
Coefficients of (42) for the case $\kappa_d = \kappa_\theta = 1, \lambda_1 > \lambda_2$

By substituting $\kappa_d = \kappa_\theta = 1$ into the expressions of $a_i, i = 1, 2$, and $b_j, j = 1, \ldots, 6$, [see (74)], we have:

$$\begin{aligned} a_2 &= \lambda_1 + \lambda_2 + \lambda_1\lambda_2\sigma_d^{-2}, \quad a_1 = \lambda_1\lambda_2\sigma_\theta^{-2} \\ b_6 &= 1, \quad b_5 = \lambda_1\sigma_d^{-2}, \quad b_4 = \lambda_2\sigma_d^{-2} \\ b_3 &= \lambda_1\lambda_2\sigma_d^{-2}\sigma_\theta^{-2}, \quad b_2 = \lambda_2\sigma_\theta^{-2}, \quad b_1 = \lambda_1\sigma_\theta^{-2} \end{aligned}$$

Thus, from (82), we conclude that in general $\beta_i \neq 0, i = 1, 2, 3$, and $\alpha_j \neq 0, j = 1, \ldots, 8$. Additionally, $\beta_3 = a_2(b_4 - g_5) = (\lambda_2 - \lambda_1)\sigma_d^{-2}a_2 < 0$, since $a_2 > 0$ and $\lambda_1 > \lambda_2$. Hence, f_1 [see (42)] is an 8th-order bivariate polynomial.

Moreover, by comparing the coefficients of (42) and (43), it is evident that χ_i, $i = 0, \ldots, 7$, are polynomials with respect to x, whose coefficients are functions of $\lambda_1, \lambda_2, c_1, c_2, \sigma_d^{-2}$, and σ_θ^{-2} [see (74) and (82)], i.e.,

$$\begin{aligned} \chi_7 &= \beta_3x \\ \chi_6 &= \alpha_7x \\ \chi_5 &= 3\beta_3x^3 + \alpha_8x^2 + \beta_2x + \alpha_3 \\ \chi_4 &= 2\alpha_7x^3 + \alpha_4x \\ \chi_3 &= 3\beta_3x^5 + 2\alpha_8x^4 + 2\beta_2x^3 + (\alpha_5 + \alpha_3)x^2 + \beta_1x \\ \chi_2 &= \alpha_7x^5 + (\alpha_6 + \alpha_4)x^3 + \alpha_1x \\ \chi_1 &= \beta_3x^7 + \alpha_8x^6 + \beta_2x^5 + \alpha_5x^4 + \beta_1x^3 + \alpha_2x^2 \\ \chi_0 &= \alpha_6x^5 \end{aligned}$$

Appendix E
Coefficients of (42) for the case $\kappa_d = 0, \kappa_\theta = 1, \lambda_1 > \lambda_2$

Substituting $\kappa_d = 0, \kappa_\theta = 1$ into the expressions of $a_i, i = 1, 2$, and $b_j, j = 1, \ldots, 6$, [see (74)], we obtain:

$$\begin{aligned} a_2 &= \lambda_1 + \lambda_2, \quad a_1 = \lambda_1\lambda_2\sigma_\theta^{-2} \\ b_6 &= 1, \quad b_5 = b_4 = b_3 = 0, \quad b_2 = \lambda_2\sigma_\theta^{-2}, \quad b_1 = \lambda_1\sigma_\theta^{-2} \end{aligned}$$

From (82), it is easy to verify that $\beta_3 = \alpha_8 = \alpha_7 = 0$, and $\beta_2 = a_2(b_1 - b_2) = (\lambda_1 - \lambda_2)(\lambda_1 + \lambda_2)\sigma_\theta^{-2} > 0$. Thus, f_1 [see (42)] can be simplified into the following 6th-order bivariate polynomial [see (47)]:

$$\begin{aligned} 0 = f_1(x, y) = \; & \beta_2xy\Delta^2 \\ & + (\alpha_6x^3 + \alpha_5x^2y + \alpha_4xy^2 + \alpha_3y^3 + \beta_1xy)\Delta + (\alpha_2x + \alpha_1y)xy \end{aligned}$$

By setting the coefficients of (47) and (48) equal, we have:

$$\begin{aligned} \zeta_5 &= \beta_2x + \alpha_3 \\ \zeta_4 &= \alpha_4x \\ \zeta_3 &= 2\beta_2x^3 + (\alpha_5 + \alpha_3)x^2 + \beta_1x \\ \zeta_2 &= (\alpha_6 + \alpha_4)x^3 + \alpha_1x \\ \zeta_1 &= \beta_2x^5 + \alpha_5x^4 + \beta_1x^3 + \alpha_2x^2 \\ \zeta_0 &= \alpha_6x^5 \end{aligned}$$

APPENDIX F
COEFFICIENTS OF (42) FOR THE CASE $\kappa_d = 1, \kappa_\theta = 0, \lambda_1 > \lambda_2$

Based on the expressions of β_3, α_8 and α_7 in (82), it is straightforward to verify that $\alpha_8 = -c_1\beta_3$ and $\alpha_7 = -c_2\beta_3$. By substituting $\kappa_d = 1, \kappa_\theta = 0$ in (74), we have:

$$a_2 = \lambda_1 + \lambda_2 + \lambda_1\lambda_2\sigma_d^{-2}, \quad a_1 = 0$$
$$b_6 = 1, \quad b_5 = \lambda_1\sigma_d^{-2}, \quad b_4 = \lambda_2\sigma_d^{-2}, \quad b_3 = b_2 = b_1 = 0$$

Substituting the above a_i, $i = 1, 2$, and b_j, $j = 1, \ldots, 6$, into (82), and recalling that $\lambda_1 > \lambda_2$, yields:

$$\beta_3 = a_2(b_4 - b_5) = (\lambda_2 - \lambda_1)\sigma_d^{-2}a_2 < 0,$$
$$\alpha_8 = -c_1\beta_3, \quad \alpha_7 = c_2\beta_3$$
$$\beta_2 = \beta_1 = \alpha_6 = \alpha_5 = \alpha_4 = \alpha_3 = \alpha_2 = \alpha_1 = 0$$

and we obtain (50):

$$0 = f_1(x, y) = \beta_3\Delta^2 xy(x^2 + y^2 - c_1x - c_2y)$$

APPENDIX G
CARTESIAN COORDINATES FOR TANGENT POINTS A & B

We hereafter determine the elements of the set $\bar{\Xi}_{1l} = \{(x, y)|\xi_1(x, y) = f_2(x, y) = 0\}$.

Clearly, $f_2 = 0$ [see (40)] describes a circle in the plane, denoted as O1, with radius r and center C, whose Cartesian coordinates are $[x_C \ y_C]^{\mathrm{T}} = \mathbf{c} = [c_1 \ c_2]^{\mathrm{T}}$ [see Fig. 3(a)]. On the other hand, by rewriting (51) as:

$$0 = \xi_1(x, y) = \left(x - \frac{c_1}{2}\right)^2 + \left(y - \frac{c_2}{2}\right)^2 - \frac{\|\mathbf{c}\|^2}{4}$$

it is straightforward to see that $\xi_1 = 0$ also corresponds to a circle O2 in the plane with radius $\frac{1}{2}\|\mathbf{c}\|$, whose center C' [see Fig. 3(a)] is the midpoint between the origin O and C, i.e., $[x_{C'} \ y_{C'}]^{\mathrm{T}} = \frac{1}{2}\mathbf{c} = \frac{1}{2}[c_1 \ c_2]^{\mathrm{T}}$. By assumption $\mathbf{c} \neq \mathbf{0}_{2\times1}$,[12] hence O2 and O1 are not concentric, which in turn implies $\bar{\Xi}_{1l}$, corresponding to the intersection of O1 and O2, has at most two elements.

Note that both O and C satisfy (51) and thus belong to O2, and since O, C', and C are on the same line, we conclude that the line segment[13] $\overline{OC}$ is the diameter of the circle O2. Moreover, since $\overline{OA}$ and $\overline{OB}$ are two tangent lines to the circle O1, intersecting O1 at A and B respectively, both triangles OAC and OBC are right triangles and share the common hypotenuse $\overline{OC}$ [see Fig. 3(a)]. Now let us focus on the right triangles OAC. Recalling that C' is the midpoint of the hypotenuse $\overline{OC}$, based on the median theorem, we conclude that $\|C'A\|$ is exactly half of $\|OC\|$, i.e., $\|C'A\| = \frac{1}{2}\|\mathbf{c}\|$. In other words, A is located on the circle whose center is C' and radius is $\frac{1}{2}\|\mathbf{c}\|$, which is precisely O2. Therefore, $A \in \bar{\Xi}_{1l}$. The same argument also applies to B. Since it has been established that $\bar{\Xi}_{1l}$ has at most two elements, we conclude that $\bar{\Xi}_{1l}$ contains exactly two real elements, which are the two tangent points A and B.

To acquire the Cartesian coordinates of A and B [see Fig. 3(a)], we first apply the Pythagorean theorem to the right triangles OAC and OBC to obtain $\|\overline{OA}\| = \|\overline{OB}\| = \tau = \sqrt{\|\mathbf{c}\|^2 - r^2}$. Note that the angles $\widehat{AOC} = \widehat{COB} = \omega = \arcsin\left(\frac{r}{\|\mathbf{c}\|}\right)$, $\widehat{XOC} = \varphi_C = \arctan\left(\frac{c_2}{c_1}\right)$, and

$$\widehat{XOA} = \widehat{XOC} - \widehat{AOC} \implies \varphi_A = \varphi_C - \omega$$
$$\widehat{XOB} = \widehat{XOC} + \widehat{COB} \implies \varphi_B = \varphi_C + \omega$$

Therefore

$$\mathbf{s}_A = \begin{bmatrix} x_A \\ y_A \end{bmatrix} = \|OA\| \begin{bmatrix} \cos\varphi_A \\ \sin\varphi_A \end{bmatrix} = \tau \begin{bmatrix} \cos(\varphi_C - \omega) \\ \sin(\varphi_C - \omega) \end{bmatrix}$$
$$\mathbf{s}_B = \begin{bmatrix} x_B \\ y_B \end{bmatrix} = \|OB\| \begin{bmatrix} \cos\varphi_B \\ \sin\varphi_B \end{bmatrix} = \tau \begin{bmatrix} \cos(\varphi_C + \omega) \\ \sin(\varphi_C + \omega) \end{bmatrix}$$

which is precisely (53).

APPENDIX H
COEFFICIENTS OF (42) FOR THE CASE $\lambda_1 = \lambda_2$

Substituting $\lambda_1 = \lambda_2 = \lambda$ into the expressions of $a_i, i = 1, 2$, and $b_j, j = 1, \ldots, 6$, [see (74)], yields:

$$a_2 = 2\lambda + \lambda^2\kappa_d\sigma_d^{-2}, \quad a_1 = \lambda^2\kappa_\theta\sigma_\theta^{-2}$$
$$b_6 = 1, \quad b_5 = b_4 = \lambda\kappa_d\sigma_d^{-2}$$
$$b_3 = \lambda^2\kappa_d\sigma_d^{-2}\kappa_\theta\sigma_\theta^{-2}, \quad b_2 = b_1 = \lambda\kappa_\theta\sigma_\theta^{-2}$$

From (82), it is easy to verify that

$$\beta_3 = \beta_2 = \beta_1 = \alpha_8 = \alpha_7 = \alpha_2 = \alpha_1 = 0$$
$$\alpha_6 = \alpha_4 = c_2\epsilon \ , \quad \alpha_5 = \alpha_3 = -c_1\epsilon$$

where

$$\epsilon = a_1(b_5 + b_6) - a_2(b_2 + b_3) = -\lambda^2\kappa_\theta\sigma_\theta^{-2}(1 + \lambda\kappa_d\sigma_d^{-2})^2$$

Thus $f_1(x, y)$ [see (42)] can be transformed into:

$$0 = f_1(x, y) = \epsilon(c_2x^3 - c_1x^2y + c_2xy^2 - c_1y^3)\Delta$$
$$= \epsilon\Delta^2(c_2x - c_1y)$$

For the single-sensor target tracking with *either* bearing-only *or* distance-and-bearing observations, $\kappa_\theta = 1$, thus $\epsilon < 0$. Additionally, $\Delta = x^2 + y^2 > 0$, hence,

$$f_1(x, y) = 0 \iff \xi_3(x, y) = c_2x - c_1y = 0$$

It is straightforward to verify that ξ_3 depicts a straight line passing through the origin O and the center C. Therefore, the critical points satisfying $f_1 = f_2 = 0$, or equivalently $\xi_3 = f_2 = 0$, must be the intersections between the line defined by $\xi_3 = 0$ and the circle described by $f_2 = 0$ [see (40)]. Hence, by referring to Fig. 3(a), the two critical points are readily attained as D and D', with $\mathbf{s}_D = \frac{\mathbf{c}}{\|\mathbf{c}\|}\big(\|\mathbf{c}\| - r\big)$ and $\mathbf{s}_{D'} = \frac{\mathbf{c}}{\|\mathbf{c}\|}\big(\|\mathbf{c}\| + r\big)$.

On the other hand, for the distance-only measurement model, $\kappa_\theta = 0$, thus $\epsilon = 0$, which yields $f_1(x, y) = 0$ regardless of x and y. Furthermore, by substituting in (32)

[12] Note that when $\mathbf{c} = \mathbf{0}_{2\times1}$, the sensor's current location coincides with the one-step-ahead target's estimated position, i.e., $\mathbf{p}_S(k) = \hat{\mathbf{p}}_T(k + 1|k)$, yielding $r = 0$. Thus, the sensor will not move and will collide with the target at the next time step, i.e., $\mathbf{p}_S(k + 1) = \hat{\mathbf{p}}_T(k + 1|k)$.

[13] $\overline{AB}$ represents the line segment with two end points A and B, while $\|AB\|$ denotes the Euclidean norm of $\overline{AB}$.

$\kappa_d = 1, \kappa_\theta = 0, \lambda_1 = \lambda_2 = \lambda$, it can be shown:

$$f_0(\mathbf{s}) = \mathrm{tr}\left(\lambda^{-1}\mathbf{I}_2 + \frac{1}{\sigma_d^2}\frac{\mathbf{s}\mathbf{s}^{\mathrm{T}}}{\mathbf{s}^{\mathrm{T}}\mathbf{s}}\right)^{-1} = \lambda + \frac{\lambda\sigma_d^2}{\lambda + \sigma_d^2} = \text{const.}$$

In other words, $f_0(\mathbf{s})$ is independent of $\mathbf{s}$, and $\nabla f_0(\mathbf{s}) = \mathbf{0}_{2\times 1},\ \forall \mathbf{s}$. Therefore, the sensor's location will not affect the trace of the target position posterior covariance for the distance-only measurement model, if $\lambda_1 = \lambda_2 = \lambda$.

Appendix I
Transforming (57) into (58)

By comparing equations (41) and (57), it is obvious that (57) is a special case of (41), obtained by choosing $\mathbf{c} = [c_1\ c_2]^{\mathrm{T}} = [0\ 0]^{\mathrm{T}}$ in (41). Thus, from (82), we conclude $\alpha_j = 0,\ j = 1, \ldots, 8$. Moreover, by substituting $\alpha_j = 0,\ j = 1, \ldots, 8$, in (42), or equivalently, setting $c_1 = c_2 = 0$ in (81), we obtain:

$$0 = xyh(\mathbf{s}^*)\big[g_y(\mathbf{s}^*) - g_x(\mathbf{s}^*)\big] \tag{83}$$

where the polynomials $h(\mathbf{s}^*),\ g_x(\mathbf{s}^*),$ and $g_y(\mathbf{s}^*)$ are defined in (77)-(79).

To acquire $g_y(\mathbf{s}^*) - g_x(\mathbf{s}^*)$, we substitute b_1, b_2, b_4, b_5 [see (74)] into (78)-(79) and attain:

$$\begin{aligned} g_y(\mathbf{s}^*) - g_x(\mathbf{s}^*) &= (\lambda_2 - \lambda_1)\big[\kappa_d\sigma_d^{-2}(x^2 + y^2) - \kappa_\theta\sigma_\theta^{-2}\big] \\ &= (\lambda_2 - \lambda_1)(\kappa_d\sigma_d^{-2}\rho^2 - \kappa_\theta\sigma_\theta^{-2}) \end{aligned} \tag{84}$$

where we have employed the equality $x^2 + y^2 = \rho^2$ [see (56)]. Note that $h(\mathbf{s}^*) > 0$, and if we assume $\lambda_1 > \lambda_2$, *and* $\kappa_d\sigma_d^{-2}\rho^2 \neq \kappa_\theta\sigma_\theta^{-2}$ (which is automatically satisfied for distance-only and bearing-only measurement models, and also holds true if $\rho \neq \frac{\sigma_d}{\sigma_\theta}$ for the distance-and-bearing observation model), then from (84), $g_y(\mathbf{s}^*) - g_x(\mathbf{s}^*) \neq 0$. Hence, (83) can be further simplified into (58), i.e., $f_4(x, y) = xy = 0$.

Appendix J
Special cases of (83)

Note that (83) remains 0 regardless of x and y, if and only if $g_x(\mathbf{s}^*) = g_y(\mathbf{s}^*)$, which [see (84)] is equivalent to *either* $\lambda_1 = \lambda_2$, *or* $\rho = \frac{\sigma_d}{\sigma_\theta}$ for $\kappa_d = \kappa_\theta = 1$.

Let us first examine $\lambda_1 = \lambda_2 = \lambda$. To proceed, we first parameterize the circle [see (56)] through its polar coordinates, i.e., $\mathbf{s} = [x\ y]^{\mathrm{T}} = \rho[\cos\varphi\ \sin\varphi]^{\mathrm{T}}$, and evaluate (32) by substituting $\mathbf{s} = \rho[\cos\varphi\ \sin\varphi]^{\mathrm{T}}$. After algebraic manipulation, we attain, for any $\mathbf{s}$ such that $\mathbf{s}^{\mathrm{T}}\mathbf{s} = \rho^2$,

$$\begin{aligned} f_0(\mathbf{s}) &= \mathrm{tr}\left(\lambda^{-1}\mathbf{I}_2 + \frac{\kappa_d}{\sigma_d^2}\frac{\mathbf{s}\mathbf{s}^{\mathrm{T}}}{\mathbf{s}^{\mathrm{T}}\mathbf{s}} + \frac{\kappa_\theta}{\sigma_\theta^2}\frac{\mathbf{J}\mathbf{s}\mathbf{s}^{\mathrm{T}}\mathbf{J}^{\mathrm{T}}}{(\mathbf{s}^{\mathrm{T}}\mathbf{s})^2}\right)^{-1} \\ &= \frac{\lambda\sigma_d^2}{\kappa_d\lambda + \sigma_d^2} + \frac{\lambda\sigma_\theta^2\rho^2}{\kappa_\theta\lambda + \sigma_\theta^2\rho^2} = \text{const.} \end{aligned}$$

In other words, $f_0(\mathbf{s})$ remains constant along the curve EGF [see Fig. 3(b)] if $\lambda_1 = \lambda_2$. Moreover, the value of this constant depends on κ_d and κ_θ.

Next, we focus on the other condition: $\kappa_d = \kappa_\theta = 1$, and $\rho = \frac{\sigma_d}{\sigma_\theta}$. To proceed, we first realize that the following identity: $\mathbf{s}\mathbf{s}^{\mathrm{T}} + \mathbf{J}\mathbf{s}\mathbf{s}^{\mathrm{T}}\mathbf{J}^{\mathrm{T}} = \big(\mathbf{s}^{\mathrm{T}}\mathbf{s}\big)^2\mathbf{I}_2$, holds true for any 2D vector $\mathbf{s}$. By substituting $\kappa_d = \kappa_\theta = 1$, $\mathbf{s}^{\mathrm{T}}\mathbf{s} = \rho^2 = \frac{\sigma_d^2}{\sigma_\theta^2}$ into (32), and employing the above identity, we obtain:

$$\begin{aligned} \mathbf{\Lambda} + \frac{1}{\sigma_d^2}\frac{\mathbf{s}\mathbf{s}^{\mathrm{T}}}{\mathbf{s}^{\mathrm{T}}\mathbf{s}} + \frac{1}{\sigma_\theta^2}\frac{\mathbf{J}\mathbf{s}\mathbf{s}^{\mathrm{T}}\mathbf{J}^{\mathrm{T}}}{(\mathbf{s}^{\mathrm{T}}\mathbf{s})^2} &= \mathbf{\Lambda} + \frac{1}{\sigma_d^2}\frac{\mathbf{s}\mathbf{s}^{\mathrm{T}}}{\mathbf{s}^{\mathrm{T}}\mathbf{s}} + \frac{1}{\sigma_d^2}\frac{\mathbf{J}\mathbf{s}\mathbf{s}^{\mathrm{T}}\mathbf{J}^{\mathrm{T}}}{\mathbf{s}^{\mathrm{T}}\mathbf{s}} \\ &= \mathbf{\Lambda} + \sigma_d^{-2}\mathbf{I}_2 \end{aligned}$$

and

$$f_0(\mathbf{s}) = \mathrm{tr}\left(\mathbf{\Lambda} + \sigma_d^{-2}\mathbf{I}_2\right)^{-1} = \frac{\lambda_1\sigma_d^2}{\lambda_1 + \sigma_d^2} + \frac{\lambda_2\sigma_d^2}{\lambda_2 + \sigma_d^2} = \text{const.}$$

Hence, $f_0(\mathbf{s})$ remains constant along the curve EGF [see Fig. 3(b)], if $\kappa_d = \kappa_\theta = 1$, and $\rho = \frac{\sigma_d}{\sigma_\theta}$.

Appendix K
Feasibility of the Critical Points

In what follows, we show that $\acute{\mathbf{s}} = [-\mathrm{sign}(c_1)\rho\ \ 0]^{\mathrm{T}}$ and $\grave{\mathbf{s}} = [0\ \ -\mathrm{sign}(c_2)\rho]^{\mathrm{T}}$ violate the maximum-speed constraint (33). To proceed, we evaluate $\|\mathbf{s} - \mathbf{c}\|$ at $\acute{\mathbf{s}}$ and $\grave{\mathbf{s}}$:

$$\begin{aligned} \|\acute{\mathbf{s}} - \mathbf{c}\|^2 &= \big(-\mathrm{sign}(c_1)\rho - c_1\big)^2 + c_2^2 = \big(\rho + |c_1|\big)^2 + c_2^2 \\ &> c_1^2 + c_2^2 = \|\mathbf{c}\|^2 \geq r^2 \\ \|\grave{\mathbf{s}} - \mathbf{c}\|^2 &= c_1^2 + \big(-\mathrm{sign}(c_2)\rho - c_2\big)^2 = c_1^2 + \big(\rho + |c_2|\big)^2 \\ &> c_1^2 + c_2^2 = \|\mathbf{c}\|^2 \geq r^2 \end{aligned}$$

Therefore $\|\acute{\mathbf{s}} - \mathbf{c}\| > r$ and $\|\grave{\mathbf{s}} - \mathbf{c}\| > r$, or equivalently, $\acute{\mathbf{s}}$ and $\grave{\mathbf{s}}$ do not satisfy the maximum-speed constraint (33).

Next, let us consider $-\acute{\mathbf{s}} = [\mathrm{sign}(c_1)\rho\ \ 0]^{\mathrm{T}}$. Clearly $-\acute{\mathbf{s}}$ automatically satisfies $\|-\acute{\mathbf{s}}\| = \rho$, hence,

$$-\acute{\mathbf{s}} \in \bar{\Omega} \iff r^2 \geq \|-\acute{\mathbf{s}} - \mathbf{c}\|^2 = \big(\rho - |c_1|\big)^2 + c_2^2$$

and by subtracting c_2^2 on both sides, we obtain (59).

Applying the same argument to $-\grave{\mathbf{s}} = [0\ \ \mathrm{sign}(c_2)\rho]^{\mathrm{T}}$,

$$-\grave{\mathbf{s}} \in \bar{\Omega} \iff r^2 \geq \|-\grave{\mathbf{s}} - \mathbf{c}\|^2 = c_1^2 + \big(\rho - |c_2|\big)^2$$

yields (60).

Appendix L
Cartesian Coordinates for Intersections E & F

The Cartesian coordinates of E and F can be derived in a similar way as A and B in Appendix G. Referring to Fig. 3(b), since the two boundary points E and F are also the intersection points of the two circles: $\|\mathbf{s} - \mathbf{c}\| = r$ and $\|\mathbf{s}\| = \rho$, we have $\|OE\| = \|OF\| = \rho$ and $\|CE\| = \|CF\| = r$. Furthermore, $\|OC\| = \|\mathbf{c}\|$. Applying the law of cosines to the triangles OEC and OFC, we obtain $\widehat{EOC} = \widehat{COF} = \varpi = \arccos\left(\frac{\rho^2 + \|\mathbf{c}\|^2 - r^2}{2\rho\|\mathbf{c}\|}\right)$. Moreover, $\widehat{XOC} = \varphi_C = \arctan\left(\frac{c_2}{c_1}\right)$, and

$$\begin{aligned} \widehat{XOE} = \widehat{XOC} - \widehat{EOC} &\implies \varphi_E = \varphi_C - \varpi \\ \widehat{XOF} = \widehat{XOC} + \widehat{COF} &\implies \varphi_F = \varphi_C + \varpi \end{aligned}$$

Thus,

$$\begin{aligned} \mathbf{s}_E = \begin{bmatrix} x_E \\ y_E \end{bmatrix} = \|OE\| \begin{bmatrix} \cos\varphi_E \\ \sin\varphi_E \end{bmatrix} = \rho \begin{bmatrix} \cos(\varphi_C - \varpi) \\ \sin(\varphi_C - \varpi) \end{bmatrix} \\ \mathbf{s}_F = \begin{bmatrix} x_F \\ y_F \end{bmatrix} = \|OF\| \begin{bmatrix} \cos\varphi_F \\ \sin\varphi_F \end{bmatrix} = \rho \begin{bmatrix} \cos(\varphi_C + \varpi) \\ \sin(\varphi_C + \varpi) \end{bmatrix} \end{aligned}$$

which is precisely (61).

REFERENCES

[1] J. Polastre, "Design and implementation of wireless sensor networks for habitat monitoring," Master's thesis, University of California, Berkeley, Berkeley, CA, May 2003.

[2] L. E. Parker, B. Birch, and C. Reardon, "Indoor target intercept using an acoustic sensor network and dual wavefront path planning," in *Proceedings of the IEEE/RSJ International Conference on Intelligent Robots and Systems*, Las Vegas, NV, Oct. 27-31 2003, pp. 278 – 283.

[3] R. Bodor, R. Morlok, and N. Papanikolopoulos, "Dual-camera system for multi-level activity recognition," in *Proceedings of the IEEE/RSJ International Conference on Intelligent Robots and Systems*, Sendai, Japan, Sep. 28 - Oct. 2 2004, pp. 643 – 648.

[4] J. Pineau, M. Montemerlo, M. Pollack, N. Roy, and S. Thrun, "Towards robotic assistants in nursing homes: Challenges and results," *Robotics and Autonomous Systems*, vol. 42, no. 3-4, pp. 271–281, Mar. 2003.

[5] G. M. Siouris, G. Chen, and J. Wang, "Tracking an incoming ballistic missile using an extended interval Kalman filter," *IEEE Transactions on Aerospace and Electronic Systems*, vol. 33, no. 1, pp. 232–240, Jan. 1997.

[6] E. J. Msechu, S. I. Roumeliotis, A. Ribeiro, and G. B. Giannakis, "Distributed quantized Kalman filtering with scalable communication cost," *IEEE Transactions on Signal Processing*, vol. 56, no. 8, pp. 3727–3741, Aug. 2008.

[7] N. Trawny and T. Barfoot, "Optimized motion strategies for cooperative localization of mobile robots," in *Proceedings of the IEEE International Conference on Robotics and Automation*, New Orleans, LA, Apr. 26 - May 1 2004, pp. 1027–1032.

[8] H. J. S. Feder, J. J. Leonard, and C. M. Smith, "Adaptive mobile robot navigation and mapping," *International Journal of Robotics Research*, vol. 18, no. 7, pp. 650–668, Jul. 1999.

[9] V. N. Christopoulos and S. I. Roumeliotis, "Adaptive sensing for instantaneous gas release parameter estimation," in *Proceedings of the IEEE International Conference on Robotics and Automation*, Barcelona, Spain, Apr. 18-22 2005, pp. 4461–4467.

[10] ——, "Multi robot trajectory generation for single source explosion parameter estimation," in *Proceedings of the IEEE International Conference on Robotics and Automation*, Barcelona, Spain, Apr. 18-22 2005, pp. 2803–2809.

[11] A. I. Mourikis and S. I. Roumeliotis, "Optimal sensor scheduling for resource-constrained localization of mobile robot formations," *IEEE Transactions on Robotics*, vol. 22, no. 5, pp. 917–931, Oct. 2006.

[12] V. Isler and R. Bajcsy, "The sensor selection problem for bounded uncertainty sensing models," *IEEE Transactions on Automation Science and Engineering*, vol. 3, no. 4, pp. 372–381, Oct. 2006.

[13] P. Yang, R. A. Freeman, and K. M. Lynch, "Distributed cooperative active sensing using consensus filters," in *Proceedings of the IEEE International Conference on Robotics and Automation*, Rome, Italy, Apr. 10-14 2007, pp. 405–410.

[14] S. Martínez and F. Bullo, "Optimal sensor placement and motion coordination for target tracking," *Automatica*, vol. 42, no. 4, pp. 661–668, Apr. 2006.

[15] E. Stump, V. Kumar, B. Grocholsky, and P. M. Shiroma, "Control for localization of targets using range-only sensors," *The International Journal of Robotics Research*, vol. 28, no. 6, pp. 743–757, 2009.

[16] J. P. Le Cadre, "Optimization of the observer motion for bearings-only target motion analysis," in *Proceedings of the 36th IEEE Conference on Decision and Control*, San Diego, CA, Dec. 10-12 1997, pp. 3126–3131.

[17] J. M. Passerieux and D. Van Cappel, "Optimal observer maneuver for bearings-only tracking," *IEEE Transactions on Aerospace and Electronic Systems*, vol. 34, no. 3, pp. 777–788, Jul. 1998.

[18] A. Logothetis, A. Isaksson, and R. J. Evans, "An information theoretic approach to observer path design for bearings-only tracking," in *Proceedings of the 36th IEEE Conference on Decision and Control*, San Diego, CA, Dec. 10-12 1997, pp. 3132–3137.

[19] ——, "Comparison of suboptimal strategies for optimal own-ship maneuvers in bearings-only tracking," in *Proceedings of the American Control Conference*, Philadelphia, PA, Jun. 24-26 1998, pp. 3334–3338.

[20] E. W. Frew, "Trajectory design for target motion estimation using monocular vision," Ph.D. dissertation, Stanford University, Stanford, CA, Aug. 2003.

[21] A. W. Stroupe and T. Balch, "Value-based action selection for observation with robot teams using probabilistic techniques," *Robotics and Autonomous Systems*, vol. 50, no. 2-3, pp. 85–97, Feb. 2005.

[22] R. Olfati-Saber, "Distributed tracking for mobile sensor networks with information-driven mobility," in *Proceedings of the American Control Conference*, New York, NY, Jul. 11-13 2007, pp. 4606–4612.

[23] T. H. Chung, J. W. Burdick, and R. M. Murray, "A decentralized motion coordination strategy for dynamic target tracking," in *Proceedings of the IEEE International Conference on Robotics and Automation*, Orlando, FL, May 15-19 2006, pp. 2416–2422.

[24] K. Zhou and S. I. Roumeliotis, "Optimal motion strategies for range-only constrained multisensor target tracking," *IEEE Transactions on Robotics*, vol. 24, no. 5, pp. 1168–1185, Oct. 2008.

[25] K. X. Zhou and S. I. Roumeliotis, "Multi-robot active target tracking with distance and bearing observations," in *Proceedings of the IEEE/RSJ International Conference on Intelligent Robots and Systems*, St. Louis, MO, Oct. 11-15 2009, pp. 2209–2216.

[26] Y. Bar-Shalom, X. R. Li, and T. Kirubarajan, *Estimation with Applications to Tracking and Navigation*. New York, NY: Wiley-Interscience, John Wiley & Sons Inc., 2001.

[27] D. P. Bertsekas, *Nonlinear Programming*, 2nd ed. Belmont, MA: Athena Scientific, 1999.

[28] D. A. Cox, J. B. Little, and D. O'Shea, *Ideals, Varieties, and Algorithms: An Introduction to Computational Algebraic Geometry and Commutative Algebra*, 3rd ed. New York, NY: Springer, 2007.

[29] A. Edelman and H. Murakami, "Polynomial roots from companion matrix eigenvalues," *Mathematics of Computation*, vol. 64, no. 210, pp. 763–776, Apr. 1995.

[30] D. P. Bertsekas and J. N. Tsitsiklis, *Parallel and Distributed Computation: Numerical Methods*. Belmont, MA: Athena Scientific, 1997.

[31] A. Ribeiro, G. B. Giannakis, and S. I. Roumeliotis, "SOI-KF: Distributed Kalman filtering with low-cost communications using the sign of innovations," *IEEE Transactions on Signal Processing*, vol. 54, no. 12, pp. 4782–4795, Dec. 2006.

[32] K. Y. K. Leung, T. D. Barfoot, and H. H. T. Liu, "Decentralized localization of sparsely-communicating robot networks: A centralized-equivalent approach," *IEEE Transactions on Robotics*, vol. 26, no. 1, pp. 62–77, Feb. 2010.

[33] E. D. Nerurkar and S. I. Roumeliotis, "Asynchronous multi-centralized cooperative localization," in *Proceedings of the IEEE/RSJ International Conference on Intelligent Robots and Systems*, Taipei, Taiwan, Oct. 18-22 2010, pp. 4352–4359.

[34] R. A. Horn and C. R. Johnson, *Matrix Analysis*. New York, NY: Cambridge University Press, 1990.

Algorithm 1 Gauss-Seidel Relaxation Algorithm

Require: $\mathbf{s}_i^{(0)} = \mathbf{c}_i,\ i = 1, \ldots, M$
Ensure: $\mathbf{s}_i = \mathbf{s}_i^{(\ell+1)},\ i = 1, \ldots, M$ {Minimize (29)}
  repeat
    for $i = 1$ to M **do**
      Calculate $\left(\mathbf{P}_i^{(\ell+1)}\right)^{-1}$ from (65)
      Determine $\mathbf{s}_i^{(\ell+1)}$ from (64) {See Algorithm 2}
      $\mathbf{s}_i^{(\ell)} \Leftarrow \mathbf{s}_i^{(\ell+1)}$ {Update $\mathbf{s}_i$}
    end for
  until max. number of iterations is reached or change in the objective function is less than 1%

Algorithm 2 Single-sensor Optimization

Require: $\lambda_1, \lambda_2, \mathbf{c}, r, \rho, \sigma_d, \sigma_\theta, \kappa_d, \kappa_\theta$
Ensure: $\mathbf{s}$ {Minimize (32), while satisfying (33)-(34)}
  if $\rho \leq \|\mathbf{c}\| - r$ **then**
    if $\lambda_1 \neq \lambda_2$ **then**
      if $\kappa_d = \kappa_\theta = 1$ **then**
        Compute $\mathbf{s}$ from (46) and (40) {See Section IV-A1}
      else if $\kappa_d = 0,\ \kappa_\theta = 1$ **then**
        Compute $\mathbf{s}$ from (49) and (40) {See Section IV-A2}
      else
        Compute $\mathbf{s}$ from (51)-(52), and (40) {See Section IV-A3}
      end if
    else
      Compute $\mathbf{s} = \frac{\mathbf{c}}{\|\mathbf{c}\|}(\|\mathbf{c}\| - r)$ {See Section IV-A4}
    end if
  else if $\sqrt{\|\mathbf{c}\|^2 - r^2} \leq \rho < \|\mathbf{c}\| + r$ **then**
    Compute $\mathbf{s}$ from (59)-(61) {See Section IV-B}
  else if $\|\mathbf{c}\| - r < \rho < \sqrt{\|\mathbf{c}\|^2 - r^2}$ **then**
    Determine $\mathbf{s}$ following the strategy outlined in Section IV-C
  else
    Compute $\mathbf{s} = \frac{\mathbf{c}}{\|\mathbf{c}\|}(r + \|\mathbf{c}\|)$ {See Section IV-D}
  end if